

Linkage among Ice Crystal Microphysics, Mesoscale Dynamics and Cloud and Precipitation Structures Revealed by Collocated Microwave Radiometer and Multi-frequency Radar Observations

Jie Gong^{1,2}, Xiping Zeng³, Dong L. Wu², S. Joseph Munchak², Xiaowen Li^{4,2}, Stefan Kneifel⁵, Davide Oris, Liang Liao^{4,2} and Donifan Barahona²

¹ Universities Space Research Association, Columbia, MD 21046, United States

² NASA Goddard Space Flight Center, Greenbelt, MD 20771, United States

³ Army Research Laboratory, Adelphi, MD 20783, United States

⁴ Morgan State University, Baltimore, MD 21251, United States

⁵ University of Cologne, Cologne 50923, Germany

Correspondence to: Jie Gong (Jie.Gong@nasa.gov)

Abstract. Ice clouds and falling snow are ubiquitous globally and play important roles in the Earth's radiation budget and precipitation processes. Ice particle microphysical properties (e.g., size, habit and orientation) are not only influenced by the ambient environment's dynamic and thermodynamic conditions, but also intimately connect to the cloud radiative effects and particle fall speeds, which therefore have an impact on future climate projection as well as on the details of the surface precipitation (e.g., onset-time, location, type and strength).

Our previous work revealed that high-frequency (>150 GHz) Polarimetric radiance Difference (PD) from passive microwave sensors is a good indicator of the bulk aspect ratio of horizontally oriented ice particles that often occur inside anvil clouds and/or stratiform precipitation. In this current work, we further investigate the dynamic/thermodynamic mechanisms and cloud/precipitation structures associated with ice-phase microphysics corresponding to different PD signals. In order to do so, collocated CloudSat radar (W-band) and Global Precipitation Measurement Dual-frequency Precipitation Radar (GPM-DPR, Ku/Ka bands) observations as well as European Centre for Medium-Range Weather Forecasts (ECMWF) atmosphere background profiles are grouped according to the magnitude of PD for only stratiform precipitation and/or anvil cloud scenes. We found that horizontally-oriented snow aggregates or large snow particles are likely the major contributor to the high-PD signals at 166 GHz, while low-PD magnitudes can be attributed to small cloud ice, randomly oriented snow aggregates, riming snow or super-cooled water. Further, high (low) PD scenes are found to be associated with stronger (weaker) wind shear and higher (lower) ambient humidity, both of which help promote (prohibit) the growth of frozen particles and the organization of convective systems. An ensemble of squall line cases is studied at the end to demonstrate that the PD asymmetry in the leading and trailing edges of the deep convection line is closely tied to the anvil cloud and stratiform precipitation layers respectively, suggesting the potential usefulness of PD as a proxy of stratiform/convective precipitation flag, as well as a proxy of convection life stage.

1 Introduction

Ice clouds and falling snow are ubiquitous. It is found that on average 50% of the surface precipitation globally is linked to ice in clouds either through the production of snow from ice crystals, or through melting of ice into rain [Field and Heymsfield, 2015]. While the primary driver of precipitation amounts is determined by the amount of water vapor available to condense and the forcing mechanism, ice microphysical processes play a key role in determining how much, and where, precipitation reaches the ground. For example, ice fall speed is closely tied to the frozen particle habit (i.e., shape), size, density, orientation, etc., and can hence influence the spatial and temporal distributions of precipitation [Milbrandt and Yau, 2006]. Studies also show that ice cloud radiative effect (CRE) is strongly dependent on ice microphysical properties [Liou et al., 2002; Tang et al., 2017; Zeng et al., 2009a, 2009b]. Therefore, it is critically important to measure, understand and appropriately incorporate ice microphysical properties in models in order to accurately capture the spatial and temporal variations of ice clouds, falling snow and surface precipitation for the sake of improving weather prediction and climate projection.

Due to the complexity and multi-faceted characteristics of ice microphysics measurements, multi-frequency radar and polarimetric radar are probably the best choices from the remote sensing point of view. For radar frequencies in millimeter to sub-millimeter regimes whose wavelengths are comparable in size to large ice to precipitating particles, the strong scattering signals and their amplitude differences at different wavelengths can provide ample information about vertical profiles of frozen particle density, particle size distribution (PSD), phase, etc. [Kneifel et al., 2011; 2015; 2016; Kulie et al., 2014; Neto et al., 2019]. Triple-frequency radar measurement techniques have been gaining attention and developed quickly in the past decade, and have been implemented at some research ground stations or field campaigns [e.g., Chase et al., 2018]. Polarimetric radar (or dual-polarization radar) measures radio wave pulses that are horizontally and vertically polarized at the same frequency. Their reflectivity difference (Z_{DR}) and specific differential phase (K_{DP}) can help better constrain the retrieval of precipitation intensity and phase discrimination.

Although active radar measurements are superb in revealing ice microphysical properties, their availability from space is limited to a curtain or narrow swaths due to mass, power and data transfer requirements. Although many ongoing efforts are pushing small-payload spaceborne radars such as RainCube Ka-band radar into space, their sensitivity, stability and reliability still require further improvements. Currently in space only CloudSat W-band radar (and EarthCare W-band radar as a successor to be launched in the near future) and Global Precipitation Measurement (GPM) Dual-frequency Precipitation Radar (DPR, Ku and Ka-bands) are operating on a regular basis, unprecedentedly deepening our understanding of ice microphysical characteristics globally [Stephens et al., 2002; Luo et al., 2008; Gettelman et al., 2010; Skofronick-Jackson et al., 2018]. However, their spatial and temporal coverages are still extremely limited (see instrument specifications in Section 2). Besides, the near-nadir views are not conducive for polarimetric measurements of ice properties.

Satellite-borne passive microwave sensors with channels suitable for measuring hydrometers have been continuously monitoring Earth's weather for more than 30 years [Manaster et al., 2017]. High-frequency microwave channel (frequency > 150 GHz) signals are dominated by frozen particle scattering when relatively thick ice clouds or frozen precipitation are present

along the line of sight, and are hence ideal for retrieving bulk ice cloud properties such as ice water path (IWP) [Gong and Wu, 2014; Eriksson et al., 2015]. Although not available on geostationary platforms, currently there are more than 10 operating polar-orbiting or procession-orbiting passive microwave sensors with channels beyond 150 GHz [GPM ATBD, 2017]. With swath width typically over 1000 km and footprint size 7-15 km, their combined usage can readily generate ice hydrometer products on temporal and spatial scales that suit the needs of both weather and climate studies.

Physically-based hydrometer retrieval algorithms are widely used to interpret the data from passive microwave sensors. In these algorithms, ice cloud profiles are estimated by accounting for the radiative transfer through frozen or liquid hydrometers as well as gas absorbers before reaching the complicated surfaces with a wide range of emissivity [e.g., Wu and Jiang, 2004 for Microwave Limb Sounder; NOAA MIRS 1D-Var retrieval system]. While some of the recent products have advanced from using spherical ice models to more realistic habits [e.g., MODIS collection 6 assumed a bulk column-aggregate shape globally for its ice cloud properties retrieval, Platnick et al., 2017; GPM products assume non-spherical but randomly oriented ice in Version 6, Ringerud et al., 2019], random orientation is still nearly always assumed to avoid the complexity of deriving size and orientation simultaneously, as well as to avoid solving equations for 4 Stokes parameters simultaneously. Ancillary data such as temperature profiles are often needed as well. To overcome these shortcomings, efforts have been put forward to use spaceborne active sensor information to help improve or constrain the errorbar of the ice hydrometer retrieval products from passive microwave sensors [e.g., Evans et al., 2012; Gong and Wu, 2014]. In particular, the GPM team uses DPR retrieved hydrometer vertical profiles as either the apriori database or “training” datasets to generate their official passive microwave and joint retrieval products [Kummerow et al., 2018; Turk et al., 2018].

Among currently available spaceborne high-frequency microwave sensors, the GPM Microwave Imager (GPM-GMI) has a unique vertically-polarized (V-pol) and horizontally-polarized (H-pol) channel pair at 166 GHz. Gong and Wu [2017] found that the magnitude of 166 GHz polarization difference (PD), defined as the brightness temperature (TB) difference between V-pol and H-pol ($PD \equiv TB_V - TB_H$), is a good indicator of the presence of oriented ice particles. The largest PDs are found in moderately cold TB (~200K), corresponding to predominately horizontally oriented ice or snow particles inside medium thick ice cloud (e.g., anvils) or stratiform precipitation layer. This feature was also identified from 85 GHz TMI (Tropical Rainfall Measuring Mission’s Microwave Imager) measurements [Prigent et al., 2005] and 157 GHz MADRAS (Megha-Tropiques’s Microwave Analysis and Detection of Rain and Atmospheric Structures) measurements [Defer et al., 2014]. In particular, Olson et al. [2011] used TMI 89 GHz PD as one of the several parameters for stratiform/convective precipitation classification. PD approaches zero for clear-sky and deep convective cores. For the former, this is because 166 GHz is not sensitive to surface polarization when column water vapor exceeds about 20mm [Zeng et al., 2019, Munchak et al., 2020]. As for the latter, Gong and Wu [2017] provided several possible explanations, including random orientation of ice particles induced by turbulent environment inside deep convective cores, large irregular-shaped graupel, or both V-pol and H-pol reach saturation at the same optical depth. Gong et al. [2017] further found that PD has a strong diurnal cycle over tropical land that is opposite to the diurnal cycle of cloud thickness and surface precipitation rate. The diurnal cycle of PD leads the latter two by ~ 2 hours, indicating that ice microphysics change over the convection life cycle, which is important to the final precipitation

100 received at the ground. Nevertheless, all of the aforementioned papers studied passive sensor signals only. Scattering signals from passive sensors have very limited information on the vertical distribution of ice particles, and hence did not answer some of the fundamental questions: **which altitude does PD information come from? What microphysical and environmental factors affect the observed PD variation over time and space? Can PD give more information in a broader context rather than just microphysics?** In this paper, these questions will be addressed by utilizing collocated GMI, DPR and
105 CloudSat radar measurements as well as auxiliary environment variables.

This paper is organized as follows. Section 2 will introduce the dataset and methodology we use to make the composites of climatology. We will present in Section 3 the differences of radar reflectivity, temperature and water vapor between high- and low-PD scenes. In Section 4, we will thoroughly discuss the underlying physical and microphysical mechanisms as well as consequences of such discrepancies. In Section 5, an ensemble of 46 squall line cases will be presented to showcase the
110 potential use of high-frequency passive microwave PD observations to differentiate precipitation system life stage. Section 6 summarizes the whole work and points out several future study directions.

2. Datasets and methodology

2.1 GPM core satellite and definition of PD regimes

The Global Precipitation Measurement (GPM) mission core satellite, launched on February 27, 2014, carries the Dual-
115 Frequency Precipitation Radar (DPR) and the GPM Microwave Imager (GMI). The GPM core satellite flies at an altitude of 407 km in a precessing orbit covering the Earth's 65°S to 65°N. DPR is composed of a Ku-band radar (KuPR) and a Ka-band radar (KaPR), making measurement at 13.6 GHz and 35.5 GHz, respectively. DPR scans cross-track with a footprint size of $\sim 5 \times 5 \text{ km}^2$ at nadir and a swath width of 245 km for KuPR and 120 km for KaPR, respectively. Both KuPR and KaPR shoot
120 49 beams in each scan with a range resolution of 250 m (over-sampled to 125 m), but 25 KaPR beams are matched with KuPR footprints for the dual-frequency algorithm to work, and the remaining 24 beams are in interlaced mode with range resolution of 250 m. Therefore, there are total three modes of DPR scanning pattern: normal scan by KuPR (NS), matched scan by KaPR (MS) and high-resolution interlaced scan by KaPR (HS)¹. In this paper, we will mainly use KuPR measurements, and the central-25 MS measurement is used whenever "KaPR" is mentioned. The 2A.GPM.DPR Version 05A measured reflectivity without attenuation correction is used in this study. More mission details can be found at Skofronick-Jackson et al. [2018;
125 2019] and GPM website at <https://gpm.nasa.gov/>.

GMI is a 13-channel conical-scan microwave radiometer that sweeps the forward-looking cone at 48.5° (Earth incident angle of 52.8°) from 10-89 GHz, and at 45° (Earth incident angle of 49.2°) from 166 to 183 GHz. Only the 166 GHz V-pol and H-pol measured brightness temperature (1B.GPM.GMI, Version 05A) will be considered in the current paper. The 166 GHz

¹ Prior to March 2018, the remaining 24 KaPR beams were interlaced at reduced vertical resolution but higher sensitivity to provide improved spatial sampling, but have since been matched to the outer swath KuPR to provide dual-frequency retrievals in the full DPR swath.

footprint size is $7.2 \times 4.2 \text{ km}^2$ (cross-track and along-track, respectively), and at this frequency the swath width is 885km on
130 the Earth's surface in the cross-track direction with 221 pixels in each scan, the center part of which overlays with DPR scan
during each GMI scan (<https://pmm.nasa.gov/gpm/flight-project/gmi>).

Gong and Wu [2017] constructed the two-dimensional probability density function (PDF) for PD-TBv relationship for different
latitude ranges; one example is shown in Fig. 1 for the deep tropics ($5^\circ\text{S} - \text{Equator}$). PD has a large spread when TB is in
the middle of the observed range, implying different cloud and precipitation regimes are likely embedded in this moderately
135 cold TB regime, which would be impossible to separate if TBv is the only metric to consider. For simplicity, we arbitrarily
define four regimes in Fig. 1: Regime #1 ($TB < 150K, PD < 5 K$) represents deep convective scenes (called "Deep
Convective Regime" hereafter); Regime #2, #3 and #4 share the same TB bounds ($150K < TB < 230K$), but different PD
ranges, namely "low-PD" ($PD < 5 K$), "medium-PD" ($5K < PD < 15 K$) and "high-PD" ($PD > 15 K$) regimes. Of course,
these thresholds are arbitrary, but those thresholds based on TBs are consistent with previous literature. For example,
140 $TB_{166\text{GHz}} < 150K$ is roughly equivalent to $TB_{85\text{GHz}} < 220K$ that was previously employed by Nesbitt et al. [2000]. This
paper will focus on the differences between "low-PD" and "high-PD" regimes, as one can imagine that the situations falling
in "medium-PD" regime must be in transition status between the "low-PD" and "high-PD" scenarios. Since the general
characteristics of the PD-TBv relationship is largely latitude-independent [Gong and Wu, 2014], this four-regime definition
can be applied globally to all GMI measurements, except there are much fewer observations falling into the deep convective
145 regime at high latitudes. Besides, shallow convection that is not as thick as deep convective cloud (e.g., congestus) may be
wrongly classified into the "low-PD" regime. However, as the total congestus area is much smaller than anvil/stratiform
precipitation areas [e.g., Zeng et al., 2018], the immixture of shallow convection structures should have negligible impact on
the general statistics.

2.2 CloudSat radar and auxiliary datasets

150 The CloudSat mission, launched on April 28, 2006 to a 705 km altitude Sun-synchronized orbit, carries the Cloud Profiling
Radar (CPR). CPR is a nadir-looking W-band (94 GHz) radar with range resolution of 240 m and footprint size of
 $1.4 \times 1.7\text{km}^2$. The measured reflectivity vertical profiles from 2B-GEOPROF Version R05 product is used in this study.

As radar frequency increases from Ku-, Ka- to W-band, the radar sensitivity window also switches from precipitation to cloud.
The CPR reflectivities are subject to strong attenuation from rain and multiple scattering from large precipitation particles.
155 This becomes a serious issue in the range bins filled with heavy precipitation (i.e., from the melting layer to the ground). Due
to complicated melting process within the melting layer, which often shows as a layer of enhancement of radar reflectivity (so-
called "bright band"), as well as the liquid attenuation issue, we will avoid discussing any reflectivity signals below 5 km
(rough height of melting layer in the tropics) for all three radars throughout the paper. Water vapor throughout the profile can
also attenuate the reflectivity signal by up to 5 dBZ for CPR [Marchand and Mace, 2018], but we still use measured reflectivity
160 to avoid introducing additional assumptions that might complicate our analysis. The impact of water vapor attenuation at W-
band will be touched upon later in the discussion.

ECMWF-AUX Version R05 dataset produced by the CloudSat team provides us auxiliary meteorological fields that are spatially and temporally interpolated to CloudSat range resolution volumes from ECMWF half-degree 3-hourly forecast data [Cronk and Partain, 2017]. Temperature, water vapor and horizontal wind profiles are compared for different PD scenarios.

165 **2.3 Collocation of radar and passive imager footprints – match and mismatch**

CloudSat-GPM Coincidence dataset Version 3B is a collection of collocated and coincident GMI, DPR and CPR measurements, which can be conveniently used for our current study. Details of collocation criteria and procedures can be found in Turk [2017]. This dataset has been used by some other researchers (e.g., Gong et al., 2017; Zeng et al., 2019). In particular, Yin et al. [2017] used collocated CPR-DPR reflectivity profiles from this dataset to study discrepancies found in
170 triple frequency radar signatures and the inferred different microphysics processes in convective and stratiform regimes. In our study, we used more than three years of data (March 2014 – October 2017) to produce a total of 3040 coincident observations globally. This number of samples is based on GMI footprint; as DPR and CPR footprint sizes are smaller, we first averaged multiple DPR and CPR profiles to one collocated GMI footprint, and then group the averaged reflectivity, temperature, water vapor, zonal and meridional wind profiles into four regimes according to the PD-TBv values. Sample sizes
175 separated in different categories can be found in Table 1. Admittedly, the sample size is strongly imbalanced between high-PD and low-PD scenes, as this is a trade-off between distinct disparities and statistical significance. Differences presented in Section 3 have passed the 95% statistical significance level unless otherwise noticed, but discussions in Section 4 are largely qualitative only.

Imperfect matching due to differences in footprint size, view-angle (i.e., atmospheric volume along line-of-sight is different
180 even when the sight lines intersect), time or other factors can distort the compiled statistics. In our case, footprint size and line of sight mismatch are likely the largest sources of bias/uncertainty due to imperfect match. On one hand, the CPR footprint is much smaller than DPR's and GMI's footprints, and therefore, any cloud/precipitation inhomogeneity in the scale smaller than ~5 km can result in discrepancies that are hard to evaluate. On the other hand, since match-up is defined to happen whenever CPR beam intercepts with DPR beam at any altitude and at any DPR view-angle, the line-of-sight volume is quite different
185 when DPR is at an off-nadir view-angle, and this problem is even more severe for GMI which always views at a slant angle. Even though a cosine function is multiplied to slightly mitigate this issue [Turk, 2017], 3D cloud inhomogeneity and beam-filling effects are again the culprit of uncertainty that is hard to justify. These two problems, however, are expected to be not too serious for our current study, because cloud inhomogeneity inside anvil and stratiform clouds is not as large as in deep convective scenes [Kirstetter et al., 2014]. Nevertheless, we know they will increase the uncertainty of our results, and temporal
190 difference (allowable to be up to 15 minutes) has a similar impact. Only footprint mismatch might add an extra bias though, as will be discussed in Section 3.1.

As this coincident dataset does not contain collocated wind and bright band information from DPR, collocated indices are matched back to CloudSat ECMWF-AUX and 2A.GPM.DPR data files to extract the wind and bright band height/width information.

195 **2.4 Radiative transfer model simulations**

To help identify the microphysical property distinctions from the observed radar reflectivities and their differences, one radiative transfer model (RTM) and another theoretical calculation are employed. The first RTM and the simulation set-up are described in detail in Leinonen and Szyrmer [2015]. An aggregation model [Leinonen, 2013] was used to generate volumetric 3-D dry and heavily rimed dendrite aggregates because of their common occurrence in the atmosphere and aggregate
200 efficiently. The particle size distribution (PSD) follows an inverse exponential distribution. The scattering computations for equivalent spheroidal snowflakes were performed using T-matrix method (TM) based on Mishchenko and Travis [1998] and Self-Similar Rayleigh-Gan theory (SSRG) method based on Hogan and Westbrook [2014]. Using these two computational methods, the dynamic range of triple-frequency diagram, which will be in Section 4, can be largely covered based on many ground observations (e.g., Kneifel et al., 2015, 2016; Kulie et al., 2014; Neto et al., 2019).

205 The second radiative transfer theoretical calculation is employed to study the density impact on the radar signal difference, which can help us diagnose which types of hydrometers likely dominate the signals under different scenarios. This model is described in detail in Liao and Meneghini [2011]. In particular, the snow follows the Gunn-Marshall size distribution [Gunn and Marshall, 1958], and rain follows the Marshall-Palmer size distribution [Marshall and Palmer, 1948]. Density and effective diameter follow a power-law form. All particles are assumed to be spheres. Simulations were verified before against airborne
210 campaign data.

3. Differences between high-PD and low-PD scenes

3.1 Radar reflectivity differences between high-PD and low-PD scenes

Using 3.5 years of collocated radar reflectivity profiles, we can composite the two-dimensional probability density function (2D-PDF) respectively from CloudSat (color shaded) and KuPR (color contours) for the four regimes for the tropics, which is
215 shown in Fig. 2. CloudSat's 2D-PDF separates "deep convective" scenario clearly from the rest three scenarios by having no bright band kink at ~ 5 km, great amount of high clouds, and the center of highest occurrence of reflectivity located in the middle-upper troposphere (7-12 km) at around 15 dBZ. The PDF of "Low-PD" scenario is the closest to that of the "deep convective" scenario among the remaining three. As PD becomes larger, the bright band kink at ~ 5 km becomes more and more distinguished while the maximum occurrence of reflectivity also shifts down toward middle troposphere (5-8 km). This
220 indicates the scene is more and more stratiform precipitation-like when PD magnitude increases. For KuPR's 2D-PDF, as Ku-band is only sensitive to the precipitation-sized particles, we basically observe the same story as with CloudSat's 2D-PDF, except KuPR cannot see high altitude anvil clouds. Because the KuPR reflectivity is barely sensitive to cloud ice-sized particles, we can also infer large ice particles high in the atmosphere in the deep convective and low PD cases, while the strong increase in reflectivity towards the bright band in the high-PD case is indicative of aggregates.

225 The 1D plots of mean reflectivity profile from CloudSat, KaPR and KuPR ingeminate the preceding story in a more clear and concise way, as shown in Fig. 3. Basically, Fig. 3 is the weighted-mean along the x-axis of Fig. 2. Since the 2A.GPM.DPR

dataset also reports the altitude of the bright band (i.e., melting layer), Fig. 3b and 3c are plotted against altitude with respect to the melting level. As we stated in Section 2, we do not intend to discuss any signals below the melting layer since CloudSat reflectivity is likely strongly attenuated below the melting layer, and measured reflectivity is used for all three radars without any attenuation or multiple scattering correction. Above the melting layer, high-level cloud (> 9 km) is thinner while middle level cloud is thicker (5-8 km) when cloud regime switches from #1 “deep convective” (dark blue) to #4 “high-PD” (red). If we check the KaPR and KuPR profiles in Fig. 3b and 3c, however, we see roughly two distinct modes: one includes scenario#1 and #2 (“deep convective” and “low PD”) that has more precipitation-sized particles throughout the upper-middle troposphere, which might imply that the convection and related cloud are still actively present within the column. On the contrary, the other mode, including scenario #3 and #4 (“medium” and “high” PDs), consist of fewer precipitation-sized particles aloft until close to the top of the melting layer due to increased temperature, where the sharp enhancement of reflectivity indicates fast and efficient growth from small ice particles to large fluffy snow aggregates. This is reasonable to happen microphysically because the sticking efficiency of two-ice-crystal collision increases rapidly near the melting layer. The latter mode might indicate the late stage of a convection life cycle, where the convective cell disappears and a stable stratiform layer forms to dominates the whole column.

Based on Fig. 2 and Fig. 3, we can summarize the discrepancies between high- and low-PD scenarios based on pure single-frequency radar observations: “low-PD” scenario has more high cloud and large ice particles high into the troposphere, implying active convective updrafts still in the development stage, while the “high-PD” scenario has much less high cloud but more middle-level cloud, with snow aggregation evident near the top of the melting layer. Therefore, “high-PD” scenario shows a distinct bright band, or melting layer signature, which is more “stratiform”-like and common in the decaying stage of convection. However, these composites are just snapshots, and without actually tracking the entire life cycle of convective system(s), these arguments need further validation. We will show some supportive evidence in Section 5 using an ensemble of squall lines. Furthermore, at this point, we cannot yet determine whether the preferably horizontally oriented large snow aggregates above the melting layer cause the “high-PD” signals, or that the randomly oriented ice/snow particles in the upper-middle troposphere effectively dampen the PD signal in the “low-PD” scenario from just looking at single-snapshot radar composites. We will discuss each of these possibilities in conjunction with radiative transfer model simulations in Section 4.

3.2 Background atmosphere differences between high-PD and low-PD scenes

In this subsection, collocation cases from tropics, mid-latitude winter, and summer are averaged separately considering they represent different weather regimes. Because CloudSat CPR is only operated in daytime mode since 2011, collocation samples over the Southern Hemisphere (SH) are very sparse (Table 1), and therefore only Northern Hemisphere (NH) winter and summer situations are shown in Fig. 4 for temperature and water vapor, and Fig. 5 for zonal and meridional winds. The definitions of extended winter (November – March) and summer (May – September) are used in order to enlarge the sample sizes. Although ECMWF-AUX, extracted from ECMWF high-resolution analysis, cannot be considered an “observation”, it is demonstrated to have high quality in capturing the mesoscale to large scale variations of atmospheric fields [Burgess et al.,

260 2013; Gong et al., 2015]. Nevertheless, due to imperfect collocation as we discussed in Section 2.3 and the fact that convection is not perfectly represented by forecast models, we would expect the ECMWF-AUX data represent both the ambient and in-cloud dynamic and thermodynamic conditions, which are unfortunately inseparable.

High and low PD regimes do not clearly differentiate from each other on the background temperature profiles as shown in Fig. 4 except for boreal winter when “high-PD” scenes are on average $\sim 10\text{K}$ warmer than the “low-PD” scenes throughout the troposphere. Water vapor amount, however, is consistently higher for “high-PD” scenes than for “low-PD” scenes in both 265 tropics and mid-latitude, which translates into higher relative humidity when temperature profiles are almost identical. In the tropics and boreal summer, widespread anvil clouds and stratiform precipitation are mostly tied to deep convective systems such as mesoscale convective system (MCS), hurricane, squall line, etc. Based on the consistent water vapor discrepancy between the two regimes, we can assert that higher humidity creates a more favorable environmental condition to promote a higher 166 GHz PD signal. Inside clouds, this feature can be understood as higher humidity usually boosts up the deposition growth of ice particles in non-convective regimes. Given the same orientation distribution, larger-sized particles will result in stronger 166 GHz PD, as shown in recent simulations by Brath et al. [2019]. Considering this difference in ambient environment, higher humidity also tends to spawn more vigorous convective systems and/or more organized convection, both of which produce vast areas of stratiform precipitation and therefore a higher 166 GHz signal.

275 The wind and wind shear differences between the two scenarios are less conclusive. Both of them are not statistically significantly differentiated from one another except for the meridional wind in boreal winter (middle panels of Fig. 5). But we can see a general pattern that both zonal and meridional low-level shears for “high-PD” scenes are higher than those for the “low-PD” scenes, which in general promotes organized convection (MCSs) with large stratiform precipitation areas. In the tropics, there is barely any wind shear for “low-PD” scenes, but “high-PD” scene exhibits stronger meridional southerly shear in the lower-level, and stronger zonal westerly shear in the upper-level. This fits into the conceptual model of mesoscale convective system (MCS) with a rear-heavy deck in that the lower-level rear inflow jet is nearly perpendicular to upper-level front-to-rear flow [Markowski and Richardson, 2010]. Weak shear in “low-PD” scenes, on the contrary, may indicate that the associated convection is either isolated, mature or dissipated so stratiform deck area is either very small or not present. For boreal summer (bottom panels of Fig. 5), the stronger lower-level wind shear in “high-PD” scenes likely promote more 285 organized convective systems or organized convective vortices, as have been shown in many modeling and observational studies [e.g., Houze, 2004; Chen et al., 2015], so “high-PD” scenes are easier to occur if they are caused by large horizontally-aligned snow aggregates that are often observed in the stratiform precipitation region. We will show in Section 5 that this hypothesis is valid for the quasi-linear MCS – Squall line situation.

In boreal winter, convection and stratiform precipitation are most frequently associated with frontal systems. The significant 290 differences in temperature ($\sim 10\text{K}$), humidity (much wetter for “high-PD” scenes) and wind (northwest wind for “high-PD” scenes versus southwest wind for “low-PD” scenes) all strongly indicate that the two scenarios correspond to two very different weather regimes. The “High-PD” environment fits the warm front region while “low-PD” environment fits the cold front and

post-frontal sectors. We will not inspect further into this speculation however, due to the page limit, and will leave this as part of the future work.

295 4. Possible causes of PD differences

Our analysis in Section 3 supports that the “high-PD” scenario is tied to a quick growth of ice particles into horizontally aligned snow particles in the middle troposphere above the melting layer. This growth process can be aggregation or water vapor/liquid deposition. However, for the “low-PD” scenario, we cannot differentiate from single radar reflectivity profiles whether the high-altitude randomly oriented large snow particles effectively damp the PD signal, or that the clouds are dominated by small
300 cloud ice particles that 166 GHz PD is insensitive to even if the particles are preferably horizontally oriented, or some other possibilities. Therefore, in this section, we will try to delineate some of the unique microphysical characteristics that are present in the “low-PD” scenario and discuss why they lead to the small PD signals at 166 GHz. This investigation will not only help us understand our particular problem more deeply, but also help explore the potential usability of PD when active radar is not present, which is most often the case.

305 As briefly introduced in Section 1, triple frequency radar reflectivity differences can reveal many quantitative structures of ice microphysical properties. In particular, Mason et al. [2019] have demonstrated that PSD shape parameter and ice morphology are the leading two factors that contribute to the spread of reflectivity differences on the triple frequency diagram, while density and axial ratio play a secondary role. However, unlike the RTM calculation and ground triple frequency radar measurements that have dedicated perfect-match design, our imperfect matches between CPR and DPR due to temporal, footprint size and
310 viewing geometry differences will confine our analysis here only to a qualitative level. But since DPR-Ku and Ka are matched, direct comparison against RTM simulations are possible, as will be shown in Fig. 7 and related discussion.

The Dual-Frequency Ratio (DFR) or Dual-Wavelength Ratio (DWR) between a pair of radar measurements is defined as the reflectivity difference when they are in dBZ units, for example, $DFR_{Ku/Ka} \equiv \frac{Reflectivity_{Ku}}{Reflectivity_{Ka}} [mm^6 m^{-3}] \equiv Z_{ku} - Z_{ka} [dBZ]$.

Two-dimensional PDFs of DFR from “high-PD” (blue contours) and “low-PD” (colored shades) scenarios using all collocated
315 samples between 5.5 – 15 km altitude range are presented on the DFR diagram in Fig. 6. Measurements below 5.5 km are excluded to avoid impacts from melting layer and potential saturation below. Because multiple radar profiles are averaged to a single GMI footprint, sensitivity thresholds are changed accordingly [Toyoshima et al., 2015]. Yin et al. [2017]’s thresholds are used here to exclude any reflectivity signals below 13, 11, and 2 dB for DPR-Ku, DPR-Ka, and CPR respectively. DFRs for two ice particle shapes (dendrite aggregate and graupel spheroid) and two riming amounts (unrimed, and heavily rimed
320 with effective liquid water path of $2kg/m^2$) are calculated and overlaid on Fig. 6b as rough references of theoretical calculated value, which are arbitrarily moved to the right by 5 dBZ in order to match the center of the observed PDFs. See Leinonen and Szyrmer [2015] for details of the RTM, scattering properties and ice morphology definitions.

$DFR_{Ku/Ka}$ does not show a significant difference between the two scenarios, but we can see a hint of slight tendency toward larger $DFR_{Ku/Ka}$ values for the “high-PD” scenario, which suggests that bigger fluffy snow aggregates are the cause of greater Ku and Ka differences. As for $DFR_{Ku/W}$ (Fig. 6a) and $DFR_{Ka/W}$ (Fig. 6b), the largest power does not center around 0 dB but at 5 dB instead, which is likely due to the different minimum detectable reflectivity for CPR and DPR [Skonfronick-Jackson et al., 2019]. This is also observed by Yin et al. [2017] for deep convective and stratiform precipitation scenes using collocated CPR-DPR measurements. Other than the biggest enhancement of power centered at 5 dB, which basically suggests that there is little difference in Ku-W and Ka-W response for most of the low-PD samples considering the disparity in their detection thresholds, there are some samples that have very large $DFR_{Ku/W}$ and $DFR_{Ka/W}$ values. These samples line up closer with the theoretical calculation for heavily rimed graupel, indicating that riming might be the cause for the low-PD signal for these samples. The two modes roughly separate at ~ 12 dB. This “double-mode” feature in $DFR_{Ku/W}$ and $DFR_{Ka/W}$ strongly suggests that “low-PD” scenarios have at least two major microphysical contributors.

To further investigate the cause of “double-mode” feature in $DFR_{Ku/W}$ and $DFR_{Ka/W}$, collocated temperature soundings at the same height level of radar reflectivity measurements are used to sort the $DFR_{Ku/Ka}$ (Fig. 7a) and $DFR_{Ku/W}$ (Fig. 7b), into four sub-categories for the “low-PD” scenario: (1) large $DFR_{Ka/W}$ (> 12 dB), cold temperature ($T < -20^\circ\text{C}$); (2) large $DFR_{Ka/W}$ (> 12 dB), warm temperature ($T > -20^\circ\text{C}$); (3) small $DFR_{Ka/W}$ (< 12 dB), cold temperature ($T < -20^\circ\text{C}$); and (4) small $DFR_{Ka/W}$ (< 12 dB), warm temperature ($T > -20^\circ\text{C}$). The temperature threshold (-20°C) roughly separates ice particles that are likely unrimed and may be partially rimed, respectively. Dias Neto et al. [2019] also found ice PSD widens toward larger DFR in the $-20^\circ\text{C} < T < -10^\circ\text{C}$ range, indicating that -20°C is a good threshold to use. The “high-PD” samples are shown as red triangles in Fig. 7. For easy reading, these four sub-categories are named as “PD_{Low}-DFR_{Large}-T_{Cold}” (light green asterisk), “PD_{Low}-DFR_{Large}-T_{Warm}” (dark green asterisk), “PD_{Low}-DFR_{Small}-T_{Cold}” (black dot), “PD_{Low}-DFR_{Small}-T_{Warm}” (blue asterisk), respectively.

Based on Fig. 7a and 7b, we can first conclude that all “high-PD” scenes (red asterisk) are within the relatively warm temperature range ($-20^\circ\text{C} < T < 0^\circ\text{C}$), which is located in the middle-low troposphere in terms of height coordinate (not shown) and hence likely consist of aggregated snow particles rather than ice cloud particles. About 50% of the “low-PD” measurements are located in the low temperature, low DFR regime (black dots). These are very likely ice cloud particles that are small and hence introduce very weak $DFR_{Ku/Ka}$, and only marginally detectable by CPR considering averaging of multiple CPR profiles onto GMI footprint significantly degrades the lower boundary of its sensitivity threshold. The rest of the “low-PD” observations (blue, light green and dark green asterisks) are inherently indistinguishable from “high-PD” ones on the $DFR_{Ku/Ka}$ axis (Fig. 7a), which indicates they are about the same size as those snow particles that generate the “high-PD” signal. However, scenes with larger $DFR_{Ka/W}$ (green asterisk) show a significantly larger $DFR_{Ku/W}$ signal too, as shown in Fig. 7b. Comparison between Fig. 7a and 7b suggests that there must be certain mechanism(s) for these large $DFR_{Ku/W}$ (or $DFR_{Ka/W}$) scenes that effectively decrease the W-band radar reflectivity. These mechanisms could be particle riming, as

355 suggested by the RTM calculations in Fig. 6b, super-cooled liquid water that works effectively as a W-band reflectivity damper
as well as 166 GHz PD damper [Xie et al., 2017], or water vapor that also impacts the W-band much more seriously than Ku
or Ka bands. According to Fig. 4, “high-PD” scenes unanimously have higher water vapor amounts than “low-PD” scenes.
Therefore, water vapor abundance could serve as a plausible explanation to explain the small $DFR_{Ku/W}$ for “high-PD” scenes
(red asterisks in Fig. 7), but not for “low-PD” scenes. Therefore, frozen particle riming and super-cooled liquid water are the
360 two most plausible candidates to explain the behaviors of those green asterisks ($PD_{Low-DFR_{Large}}$). For $PD_{Low-DFR_{Small}}$ scenes
(black dot and blue asterisks), we have discussed that black dot scenes probably correspond to cloud ice particles because of
cold temperature and relatively high altitude where they are located, and the blue asterisks scenes may be explained as
randomly oriented unrimed snow aggregates.

Particle density isolines overlaid on DFR-Z plots can help further delineate the different microphysical regimes that “high-
365 PD” and “low-PD” scenarios fall into, as shown in Fig. 7c and 7d. These isolines are replicated from the same scattering model
and set-ups of Liao and Meneghini [2011]. Keep in mind that Fig. 7c is comparable quantitatively to the theoretical isolines
(other than that the water vapor is not corrected) as Ku-Ka are perfectly matched in beam, while 7d can only assist our
interpretation qualitatively. The “high-PD” scenes are separated from the three “low-PD” sub-categories in Fig. 7c, and more
clearly in Fig. 7d ($PD_{Low-DFR_{Small-T_{cold}}$ samples, the black dots in Fig. 7a and 7b, are not shown because they are likely from
370 cloud ice particles). In particular, one can see that given the same small DFR, the blue asterisks are generally denser than red
triangles. This agrees with our earlier hypothesis that the “high-PD” is mainly induced by fluffy snow aggregates where ice
crystals are loosely attached to each other during the rapid aggregation process, and therefore tend to fall slowly and orient
horizontally because of the large geometric area. On the other hand, some of the “low-PD” signals (blue asterisks) are induced
by denser snow aggregates that are comparable in effective diameter with those ones in the “high-PD” scenes. However,
375 because the ice crystals are more tightly collided together in these snow aggregates, they tend to not have a preferred shape or
orientation. The dark green asterisks are suggested by Fig. 7c to be even denser (except a few outliers on the top-right corner),
which strongly suggest that they are possibly experiencing riming. Fig. 7d tells contradictory story about these green asterisks,
however. But noting that observations in Fig. 7d are not directly comparable with RTM calculations because of imperfect
volume matching, we focus on and trust more the results presented in Fig. 7c (and similarly Fig. 7a).

380 To summarize this section, we are able to provide more evidences that the “high-PD” signal is mainly induced by horizontally
oriented fluffy snow aggregates, while also successfully delineating several possible microphysical mechanisms of “low-PD”
signals, which are: (1) small cloud ice particles; (2) more densely aggregated snow particles that tend to orient randomly; (3)
riming snow; (4) super-cooled liquid water. This section demonstrates the value and importance of closely matched triple
frequency radar measurements in conjunction with accurate atmospheric soundings. We also find that 166 GHz PD indeed is
385 primarily sensitive to the orientation of large snow particles instead of small cloud ice particles. Adding polarization
measurements at a sub-mm frequency (e.g., 640 GHz from Ice Cloud Imager sensor) may likely aid in disentangling orientation
of cloud ice from that of snow particles from a passive sensor.

5. PD variations through cloud-precipitation life stage: demonstration with squall lines

Convective systems usually experience a complete life cycle of development. During the developing stage, the deep convective
390 tower(s) quickly shoots up and anvil deck quickly spreads out. During the decaying stage, the convective core dissipates and
is replaced with a stable stratiform precipitating area. By far it is established that the leading anvil cloud is likely associated
with low-PD, while high-PD is likely associated with a trailing stratiform layer. Can we then use PD as a proxy to tell which
stage a convective system is at? If yes, does high-PD necessarily imply more intense surface precipitation compared to low-
PD regime given the same TB range? In this section, we will explore the potential usefulness of PD on a relatively simple
395 natural testbed – squall line system. Squall lines, as a subset of typical convective systems, are an ideal testbed because they
are quasi-linear (i.e., no rotation like hurricanes or frontal systems), and the anvil head in the leading edge and the vast area of
stratiform precipitation layer in the trailing edge are easily separable on GMI images.

We manually selected 46 squall line cases from GPM observations (see Table A1 for detailed location, orbit number and date).
For these 46 cases, we require: (1) the line of deep convection must be captured by DPR; and (2) the squall line moving
400 direction must be quasi-perpendicular to GPM orbit. The latter requirement assures that each GMI conical scan can slice
through the squall line whenever the collocated DPR captures a deep convective core. An example of a selected case is given
in Fig. 8, where the leading edge and trailing edge is to the left and right, respectively, because this case happened over Sahel.
From Fig. 8b we can clearly visualize that PD is significantly higher behind the line of deep convection identified from Fig.
8c on the DPR image. To composite the ensemble of 46 cases together, we first identify the footprint location on each DPR
405 scan that has the maximum Ku-PR retrieved near-surface precipitation rate (PR_{sfc}), which is required to be beyond a threshold
($PR_{sfc} > 25 \text{ mm/h}$). This threshold is arbitrarily set, but works robustly against a range of values ($20 - 50 \text{ mm/h}$ are tested,
and only the number of qualified samples are changed without altering the conclusion). The location of identified deep
convective centers are shown in Fig. A1. Once the center of convection on a DPR scan is identified, the collocated GMI
footprint and its index on the scan are then pin-pointed. Next, the footprints corresponding to the leading edge and trailing
410 edge are sorted accordingly against the convective center. Lastly, all selected GMI and DPR scans are aligned together with
GMI's deep convective center footprint in the middle, trailing edge to the left and leading edge to the right. The averaged
cross-section of 166 GHz TB and PD responses for each case are shown as black lines in Fig. 9a and 9b, respectively, while
the ensemble means are the red bold lines. The DPR scan widths are shown as light grey rectangles in Fig. 9a and 9b for
comparison.

415 Both TB and PD across the squall line are asymmetric about the deep convective center. The ensemble mean of TB is $\sim 10 \text{ K}$
colder to the trailing edge than to the leading edge, which translates into a radiatively thicker anvil cloud/falling snow layer
behind the squall line than ahead of it. The width of depression of TB is also much broader in the trailing edge than in the
leading edge. Both features agree well with our conceptual picture of squall line system [Houze, 2004]. Cetrone and Houze
[2011] selected and studied another ensemble of Africa squall lines, and they found that the geometric thicknesses of leading

420 anvil and trailing stratiform cloud layers are not significantly different. So a radiative thickness difference of ~ 10 K in our ensemble case could indicate larger snow particles in the trailing edge than fresh anvil cloud ice particles in the leading edge. The ensemble mean of PD, as expected, displays a double-peak in front and behind the deep convective center. The peak occurs ~ 70 km and ~ 25 km away from the center on the trailing edge and leading edge, respectively. The magnitude of PD in the trailing edge is apparently larger (7 K) and spread more wildly than that in the leading edge (5.5 K). Interestingly, PD
425 in the deep convection is not zero but ~ 4.5 K. One can see from the general statistics in Fig. 1 that PD is ~ 4 K when TB is about 120 K, which are consistent with the mean TB and PD values we found for deep convective cores from our squall line ensemble. We can further see from Fig. 10b when the distribution of PD is plotted that discernable number of convective pixels have large PD values and hence skewed the mean toward the positive side. A 5.5 K peak PD value in the leading edge suggests that there are also significant amount of large horizontally-aligned ice particles inside leading anvil decks, which is consistent
430 with previous findings in Cetrone and Houze [2011].

The $PR_{sfc} - PD$ relationship is further evaluated. We perform this evaluation from two perspectives. First, we would like to check if across the squall line, precipitation intensity is significantly different or not, and whether it's related to the magnitude of PD. A threshold of 5 mm/h is used as a rough threshold to exclude convective rain scenes because the magnitude of PD inside convection involves too many complicated dynamic/microphysical processes and this is not what this paper is aiming
435 for. Away from the convection, a correlation of 0.77 (significant at 99.9% confidence level) is achieved, as shown in Fig. 9c. PR_{sfc} reaches 2 mm/h in the stratiform zone behind the deep convection, which is < 1 mm/h in the leading edge. Considering that it takes some time for snow aggregates to fall down to the surface while squall line keeps on moving forward, a spatially lagged correlation would be more physically meaningful [Gong et al., 2017]. Unfortunately, the DPR scan is too narrow for us to conduct such a lag-correlation test. The other way to evaluate the $PR_{sfc} - PD$ relationship is to composite the statistics.
440 Since Level 2 DPR retrievals provide the precipitation type flag, which classify precipitation into three types: stratiform, convective and other, we use these three flags to separate our ensemble data into three categories, and composite the 2D PDF of $PR_{sfc} - PD$ for each of them. Note that "stratiform precipitation" flag only occurs in the trailing edge, but "other precipitation" flag may include precipitation happening everywhere within the domain, so we add an extra criterion that only the footprints located at the leading edge are selected to use. The 2D PDF composites of $PR_{sfc} - PD$ for stratiform, deep
445 convective and leading edge are shown in Fig. 10, which are completely different, confirming that the cloud-precipitation process belongs to completely different regimes for each of the three types. The maximum likelihood of PD in the stratiform region reaches ~ 10 K, while in convective regime it centers around 4-6 K, and the value spreads out in the leading edge from as small as 2 K to up to 10 K. PD is only positively correlated with surface precipitation rate in the stratiform region and only when PD is high. A 2 K increase of PD from 8 K to 10 K corresponds to a four-fold increase of PR_{sfc} from 1 mm/h to 4 mm/h
450 (note that the horizontal axis in Fig. 10 is logarithmic), which is quite remarkable and again demonstrates the importance of ice microphysics to the local precipitation intensity and its variation. In the convective regime, PD is weakly negatively correlated with surface precipitation, but when PD is large (> 8 K roughly), the correlation becomes negligible or even positive,

which is likely due to the fact that these pixels are close to the boundary of convective-stratiform separation. Keep in mind that these correlations (Fig. 10) can only be performed within the narrow DPR swath (grey bars in Fig. 9a and 9b) where both
455 DPR identified precipitation flag and collocated 166 GHz PD measurements are available, while the majority of stratiform precipitation and fresh anvil leading head are outside of the DPR swath using our current ensemble technique, so Fig. 10 is just looking at a spot of the leopard, and more comprehensive works are needed in the future to recover the whole picture.

Although the steep slope means that PR_{sfc} is very sensitive to the magnitude of PD in the stratiform region when PD is large, the overall spread of the 2D PDF suggests that we cannot incautiously use PD as a new parameter for surface precipitation
460 retrieval. Rather, this finding suggests that 166 GHz PD could be and should be considered as an extra constraint to GMI-only precipitation retrieval because of its added value in certain regimes, which remains as a worthwhile topic for future exploration. Meanwhile, we can clearly see from Fig. 10c that in non-stratiform regimes (i.e., leading edge in our squall line cases), PD is not correlated with PR_{sfc} at all. The contrast of 2D PDF shapes in the trailing edge versus in the leading edge again goes along with our understanding that large horizontally aligned snow aggregates tend to occur in the stratiform layer and tend to
465 precipitate down in a short frame of time, while it takes longer time for those relatively small snowflakes hanging up in the fresh anvil deck in the leading edge to fall to the ground, the latter of which apparently will enjoy varied experiences during the falling process. Furthermore, PD from 166 GHz cannot be used solely to diagnose the life stage of convective system either, but multiple spaciouly coherent PD measurements spanning from MW to sub-mm or even infrared spectra may realize this function eventually without any involvement of active remote sensing. For example, Olson et al. [2001] developed a
470 passive MW-only flag system, called “convective-stratiform index (CSI)”, to flag out convective and stratiform scenes, which relies on a combination use of TB and TB gradient at 19, 37 and 85 GHz, as well as 85 GHz PD magnitude. This was back in TRMM era when 85 GHz is the highest available frequency making measurements at both V-pol and H-pol. Although not shown nor discussed in the main text, Fig. A2 includes the same squall line ensemble of TB and PD at 89 GHz from GMI measurements. We can see that 89 GHz PD spreads all over the place and does not show a good correspondence to deep
475 convective or stratiform zones (Fig. A2 in the Appendix). Based on our investigation in this paper, 166 GHz PD is likely a better candidate to update the CSI algorithm, which is left for exploration in the future.

6. Conclusions and Future Works

At 166 GHz, GMI currently makes the highest frequency of dual-polarized microwave radiance measurements from space. Gong and Wu [2017] and Gong et al. [2017] thoroughly studied the PD and TB signals from GMI, and laid out several possible
480 microphysical mechanisms that can explain the PD signal under different TB regimes. In this paper, leveraging the collocated DPR and CPR radar reflectivity measurements, we are, for the first time, able to delineate the microphysical properties not only for high-PD scenes, but also for low-PD scenes for the same moderately-cold TB regime. As high-frequency MW radiance measurements can only be used to infer column-integrated mass quantities such as ice water path for this moderately-cold TB regime, the PD measurement allows us to diagnose much more information about the microphysical processes occurring in

485 the profile. The analysis of PD and radar data in this paper suggests that 166 GHz PD is closely associated with horizontally oriented large fluffy snow aggregates in the stratiform precipitation layers that tends to melt and fall as precipitation soon. Low 166 GHz PD signals, however, are associated with more complicated situations. At least four mechanisms are found possibly responsible for the low PD signals: (1) small cloud ice particles up aloft that 166 GHz PD is barely sensitive to; (2) more densely aggregated snow particles that tend to orient randomly; (3) riming snow particles that effectively damp the PD signal; 490 (4) super-cooled liquid water that also damps the PD signal. With only 166 GHz TB and PD observations, it is difficult to distinguish which mechanism dominates a single scene, but better diagnostic approaches can be developed in the future using adjacent passive-only observations in conjunction with accurate atmospheric background measurements or analysis. As sub-millimeter radiances are more sensitive to smaller particles, multi-frequency PD measurements at MW and sub-mm spectra can be provided the best approach to separate particle size, shape and orientation information from cloud ice and snow aggregates, as already shown via RTM simulations by Brath et al. [2019].

This paper also demonstrates the value of using collocated triple-frequency radar measurements to disentangle the complicated microphysical characteristics along the passive MW line of sight. However, due to beam-filling and other mis-match issues (e.g., footprint, view-angle and temporal disparities), our “pseudo-triple-frequency” radar (DPR+CPR) statistics are distorted and displaced, and therefore cannot be directly compared with RTM simulations quantitatively. Since perfectly matched triple- 500 frequency radar space mission will be likely unavailable in the near future, using collocated ground or “pseudo-collocated” space radar measurements together with passive MW PD observations are probably the best approach to extend our knowledge about passive MW PD signals for a better scientific and/or operational use. Besides DFR, other parameters should also be inspected in the future work. For example, dual-wavelength ratio (DWR) can provide information on ice particle size without being influenced by particle concentration.

505 We lastly scrutinized 166 GHz PD and DPR behaviors in an ensemble of squall line cases. We found out that PD is larger in the trailing edge where large snow aggregates are predominant in the stratiform layer, while PD is smaller in the leading edge where fresh anvil decks dominate the scene. Surface precipitation, as expected, is positively correlated with PD in the stratiform region when high-PD occurs. Three possible ways of using PD are then discussed, which are: (1) using 166 GHz PD to constrain passive-only surface precipitation retrieval under certain conditions; (2) using multi-frequency PD and TB 510 measurements to help diagnose the life stage of convective system; (3) improving the design of passive-only stratiform/convective precipitation flags. They will be explored in the future.

Acknowledgement

We are grateful to the dedicated experts from CloudSat and GPM teams who maintain and distribute the high scientific-quality Level 1 and Level 2 data. We are in particular in debt to GPM precipitation feature product producer Dr. Chuntao Liu at Texas 515 A&M Corpse Christi. Discussions with Drs. Manfred Brath, Ian Adams and Chuntao Liu, among others, greatly help make this paper a better shape. This work is mainly conducted under the support from NASA Grant# 80NSSC20K0087. Funding

supports from Grant#NNX16AM06G and NASA ROSES NNH18ZDA001N-RRNES are also highly appreciated. Drs. D. Ori and S. Kneifel acknowledge funding from the German Research Foundation (DFG) under grant KN 1112/2-1 as part of the Emmy-Noether Group Optimal combination of Polarimetric and Triple Frequency radar techniques for Improving
520 Microphysical process understanding of cold clouds (OPTIMIce).

Author Contributions

Dr. Gong and Dr. Munchak initiated the original idea. Dr. Gong conducted most of the data analysis and results interpretation. Dr. Munchak provided part of the Ku/Ka CFAD composites. Dr. Zeng, Dr. Wu and Dr. Li were heavily involved in interpreting
525 the results. In addition, Dr. Li provided the squall line ensemble cases. Drs. Kneifel and Ori provided the theoretical calculations of the triple frequency radar DFR and helped on explaining some of the observational property. Dr. Liang provided the theoretical calculations of the density isolines. Dr. Barahona provided the global model perspective for this study.

Data Distribution

GPM data and collocated GPM-CPR data are available to public at NASA PPS FTP at <https://pmm.nasa.gov/data-access/downloads/gpm>. CloudSat and ECMWF-AUX data are made available from CloudSat FTP at
530 <http://www.cloudsat.cira.colostate.edu/order-data>. High/low PD statistics can be provided to readers upon request.

Competing Interests Disclaimer

The authors claim no competing interests against any institutions or individuals.

References

- 535 Brath, M., R. Ekelund, P. Eriksson, O. Lemke, and S. A. Buehler (2019), Microwave and submillimeter wave scattering of oriented ice particles, *Atm. Meas. Tech. Diss.*, doi:10.5194/amt-2019-382
- Burgess, B. H., A. R. Erler, and T. G. Shepherd (2013), The troposphere-to-stratosphere transition in kinetic energy spectra and nonlinear spectral fluxes as seen in ECMWF analyses. *J. Atmos. Sci.*, 70, 669–687, doi:https://doi.org/10.1175/JAS-D-12-0129.1
- 540 Cetrone, J. and R. A. Houze (2011), Leading and Trailing Anvil Clouds of West African Squall Line, *J. Atmos. Sci.*, doi: 10.1175/2011JAS3580.1.

- Chase, R. J., J. A. Finlon, P. Borque, G. M. McFarquhar, S. W. Nesbitt, S. Tanelli, O. O. Sy, S. L. Durden, M. R. Poellot (2018), Evaluation of triple-frequency radar retrieval of snowfall properties using coincident airborne in situ observations during OLYMPEX, *Geophys. Res. Letts.*, doi:10.1029/2018GL077997.
- 545 Chen, Q., J. Fan, S. Hagos, W. Gustafson Jr., L. K. Berg (2015), Roles of wind shear at different vertical levels: cloud system organization and properties, *J. Geophys. Res. – Atm.*, doi:10.1002/2015JD023253.
- Cronk, H. and P. Partain (2017), CloudSat ECMWF-AUX Auxillary data product process description and interface control document, http://www.cloudsat.cira.colostate.edu/sites/default/files/products/files/ECMWF-AUX_PDICD.P_R05.rev0_.pdf.
- Defer, E., V. S. Galligani, C. Prigent, and C. Jimenez (2014), First observations of polarized scattering over ice clouds at close-
550 to-millimeter wavelengths (157 GHz) with MADRAS on board the Megha-Tropiques mission, *J. Geophys. Res.: Atmospheres* 119.21, 2014JD022353. doi: 10.1002/2014JD022353.
- Dias Neto, J., S. Kneifel, D. Ori, S. Trömel, J. Handwerker, B. Bohn, N. Hermes, K. Mühlbauer, M. Lenefer, and C. Simmer (2019), The TRiple-frequency and Polarimetric radar Experiment for improving process observations of winter precipitation, *Earth Syst. Sci. Data*, 11, 845–863, 2019, <https://doi.org/10.5194/essd-11-845-2019>.
- 555 Field, P. R., and Heymsfield, A. J. (2015), Importance of snow to global precipitation, *Res. Lett.*, 42, 9512–9520, DOI:10.1002/2015GL065497
- Eriksson, P., M. Jamali, J. Mendrok, and S. A. Buehler (2015), On the microwave optical properties of randomly oriented ice hydrometeors, *Atm. Meas. Tech.*, doi:10.5194/amt-8-1913-2015.
- Evans, K.F., J. R. Wang, D. O’C Starr, G. Heymsfield, L. Li, L. Tian, R. P. Lawson, A. J. Heymsfield, and A. Bansemmer
560 (2012), Ice hydrometeor profile retrieval algorithm for high frequency micro-wave radiometers: application to the CoSSIR instrument during TC4, *Atmos. Meas. Tech.*, 5, 2277-2306. doi:10.5194/amt-5-2277- 2012.
- Gong, J., and D. L. Wu (2014), CloudSat-constrained cloud ice water path and cloud top height retrievals from MHS 157 and 183 GHz radiances, *Atmos. Meas. Tech.*, [doi: 10.5194/amt-7-1873-2014].
- Gong, J., J. Yue, and D. L. Wu (2015), Global survey of concentric gravity waves in AIRS images and ECMWF analysis, *J.*
565 *Geophys. Res. Atmos.*, 120, 2210– 2228, doi:10.1002/2014JD022527.
- Gong, J., and D. L. Wu (2017), Microphysical Properties of Frozen Particles Inferred from Global Precipitation Measurement (GPM) Microwave Imager (GMI) Polarimetric Measurements. *Atmospheric Chemistry and Physics*, 17: 2741-2757.
- Gong, J., X. Zeng, D. L. Wu, and X. Li (2017), Diurnal Variation of Tropical Ice Cloud Microphysics: Evidence from Global Precipitation Measurement Microwave Imager (GPM-GMI) Polarimetric Measurements. *Geophysical Research Letters*,
570 [10.1002/2017gl075519].
- Gettleman, A., X. Liu, S. J. Ghan, H. Morrison, S. Park, A. J. Conley, S. A. Klein, J. Boyle, D. L. Mitchell, J.-L. F. Li (2010), Global siulations of ice nucleation and ice supersaturation with an improved cloud scheme in the Community Atmosphere Model, *J. Geophys. Res. – Atm.*, doi:10.1029/2009JD013797.
- Hogan, R. J., and C. D. Westbrook (2014), Equation for the microwave backscatter cross section of aggregate snowflakes
575 using the self-similar rayleigh-gans approximation, *J. Atmos. Sci.*, 9, 3292– 3301.

- Houze Jr., R. A. (2004), Mesoscale Convective Systems, Review of Geophysics, doi: 10.1029/2004RG000150.
- Kneifel, S., M. S. Kulie, R. Bennartz (2011), A triple-frequency approach to retrieve microphysical snowfall parameters, *J. Geophys. Sci.*, doi: 10.1029/2010JD015430.
- Kirstetter, P.-E., Y. Hong, J. J. Gourley, M. Schwaller, W. Petersen, and Q. Cao (2014), Impact of sub-pixel rainfall variability on spaceborne precipitation estimation: evaluating the TRMM 2A25 product, *Quant. J. Royal. Meteor. Soc.*, 10.1002/qj2416.
- Kneifel, S., A. v. Lerber, J. Tiira, D. Moisseev, P. Kollias, J. Leinonen (2015), Observed relations between snowfall microphysics and triple-frequency radar measurements, *J. Geophys. Sci.*, doi: 10.1002/2015JD023156.
- Kneifel, S., P. Kollias, A. Battaglia, J. Leinonen, M. Maahn, H. Kalesse, F. Tridon (2016), First observations of triple-frequency radar Doppler spectra in snowfall: interpretation and applications, *Geophys. Res. Lett.*, doi:10.1002/2015GL067618.
- Kollias, P. B. Albrecht (2005), Why the melting layer radar reflectivity is not bright at 94 GHz? *Geophys. Res. Lett.*, doi:10.1029/2005GL024074.
- Kulie, M. S., M. J. Hiley, and R. Bennartz (2014), Triple-frequency radar reflectivity signatures of snow: observations and comparisons with theoretical ice particle scattering models, *J. Appl. Meteor. And Clim.*, doi: 10.1175/JAMC-D-13-066.1.
- Kummerow, C. D., D. L. Randel, M. Kulie, N.-Y. Sang, R. Ferraro, S. J. Munchak and V. Petkovic (2018), The evolution of the Goddard profiling algorithm to a fully parametric scheme, *J. Atm. And Ocn. Tech.*, doi:10.1175/JTECH-D-15-0039.1.
- Leinonen, J., W. Szyrmer (2015), Radar signatures of snowflake riming: a modeling study, *Earth and Space Science*, doi:10.1002/2015EA000102.
- Liao, L., and R. Meneghini (2011), A study on the feasibility of dual-wavelength radar for identification of hydrometeor phases. *J. Appl. Meteorol. Climatol.*, 50, 449–456.
- Luo, Z., G. Y. Liu, G. L. Stephens (2008), CloudSat adding new insight into tropical penetrating convection, *Geophys. Res. Lett.*, doi: 10.1029/2008GL035330.
- Manaster, A., C. W. O'Dell, G. Elsaesser (2017), Evaluation of cloud liquid water path trends using a multidecadal record of passive microwave observations, *J. Clim.*, doi:10.1175/JCLI-D-16-0399.1.
- Mishchenko, M. I., and L. D. Travis (1998), Capabilities and limitations of a current FORTRAN implementation of the T-matrix method for randomly oriented, rotationally symmetric scatterers, *J. Quant. Spectros. Radiat. Transfer*, 60(3), 309–324, doi:[10.1016/S0022-4073\(98\)00008-9](https://doi.org/10.1016/S0022-4073(98)00008-9).
- Marchand, R., G. Mace (2018), Level 2 GEOPROF product process description and interface control document, P1_R05, http://www.cloudsat.cira.colostate.edu/sites/default/files/products/files/2B-GEOPROF_PDICD.P1_R05.rev0__0.pdf.
- Markowski, P. and Y. Richardson (2010), Mesoscale meteorology in midlatitudes, Chapter 9, mesoscale convective systems, ISBN: 978-0-470-74213-6.
- Mason, S. L., R. J. Hogan, C. D. Westbrook, S. Kneifel, D. Moisseev, and L. v. Terzi (2019), The importance of particle size distribution and internal structure for triple-frequency radar retrievals of the morphology of snow, *Atmos. Meas. Tech.*, doi:10.5194/amt-12-4993-2019.

- Milbrandt, J. A., and M. K. Yau (2006), A multimoment bulk microphysics parameterization. Part IV: Sensitivity experiments. *J. Atmos. Sci.*, 63, 3137–3159, <https://doi.org/10.1175/JAS3817.1>.
- NASA Goddard Space Flight Center PPS and GPM Intercalibration Working Group (2017), Algorithm Theoretical Basis Document (ATBD), NASA GPM Level 1C Algorithms, Version 1.8, https://pps.gsfc.nasa.gov/Documents/L1C_ATBD.pdf.
- Neto, D. J., S. Kneifel, D. Ori, S. Tromel, J. Handwerker, B. Bohn, N. Hermes, K. Muhlbauer, M. Lenefer, and C. Simmer (2019), The triple-frequency and polarimetric radar experiment for improving process observations of winter precipitation, *Earth Sys. Sci. Data*, doi:10.5281/zenodo.1341389.
- Nesbitt, S. W., E. J. Zipser, D. J. Cecil (2000), A Census of Precipitation Features in the Tropics Using TRMM: Radar, Ice Scattering, and Lightning Observations, *J. Clim.*, [https://doi.org/10.1175/1520-0442\(2000\)013<4087:ACOPFI>2.0.CO;2](https://doi.org/10.1175/1520-0442(2000)013<4087:ACOPFI>2.0.CO;2)
- Olson, W. S., Y. Hong, C. D. Kummerow, and J. Turk (2001), A texture-polarization method for estimating convective-stratiform precipitation area coverage from passive microwave radiometer data, *J. Appl. Meteor. and Clim.*, doi:10.1175/1520-0450(2001)040<1577:ATPMFE>2.0.CO;2
- Platnick, S. *et al.* (2017), The MODIS Cloud Optical and Microphysical Products: Collection 6 Updates and Examples From Terra and Aqua, in *IEEE Transactions on Geoscience and Remote Sensing*, vol. 55, no. 1, pp. 502-525, doi: 10.1109/TGRS.2016.2610522.
- Prigent, C., E. Defer, J. Pardo, C. Pearl, W. B. Rossow, and J.-P. Pinty (2005), Relations of polarized scattering signatures observed by the TRMM Microwave Instrument with electrical processes in cloud systems, *Geophys. Res. Lett.*, 32, L04810, doi:10.1029/2004GL022225.
- Ringerud, S., Kulie, M. S., Randel, D. L., Skofronick-Jackson, G. M., & Kummerow, C. D. (2019). Effects of ice particle representation on passive microwave precipitation retrieval in a Bayesian scheme. *IEEE Transactions on Geoscience and Remote Sensing*, 57(6), 3619-3632.
- Simmons, K. M. and D. Sutter (2005), WSR-88D radar, tornado warnings and tornado casualties, *Weather and Forecasting*, doi:10.1175/WAF857.1.
- Skofronick-Jackson, G., D. Kirschbaum, W. Petersen, G. Huffman, Chris Kidd, Erich Stocker, R. Kakar (2018), The global precipitation measurement (GPM) mission’s scientific achievements and societal contributions: reviewing four years of advanced rain and snow observations, *Royal Meteor. Soc.*, doi:10.1002/qj.3313.
- Skofronick-Jackson, G., M. Kulie, L. Milani, S. J. Munchak, N. B. Wood, and V. Lavizzani (2019), Satellite Estimation of Falling Snow: A Global Precipitation Measurement (GPM) Core Observatory Perspective, *J. Appl. Meteor. Clim.*, <https://doi.org/10.1175/JAMC-D-18-0124.1>.
- Stephens, G. L., D. G. Vane, R. J. Boain, G. G. Mace, K. Sassen, Z. Wang, A. Illingworth, E. J. O’connor, W. B. Rossow, S. L. Durden, S. D. Miller, R. T. Austin, A. Benedetti, C. Mitrescu, and the CloudSat Science Team (2002), A new dimension of space-based observations of clouds and precipitation, *B.A.M.S.*, doi:10.1175/BAMS-83-12-1771.
- Teschl, F., W. L. Randeu, and R. Teschl (2013), Single-scattering of preferentially oriented ice crystals at centimeter and millimeter wavelengths, *Atmos. Res.*, 119, 112-119, doi.org/10.1016/j.atmosres.2011.10.004

- Toyoshima K, Masunaga H, Furuzawa FA (2015), Early Evaluation of Ku- and Ka-Band Sensitivities for the Global Precipitation Measurement (GPM) Dual-Frequency Precipitation Radar (DPR), *Scientific Online Letters on the Atmosphere*, doi.org/10.2151/sola.2015-004.
- 645 Turk, J. (2017). CloudSat-GPM coincidence dataset, Algorithm and Theoretical Basis Document, https://pps.gsfc.nasa.gov/Documents/CSATGPM_COIN_ATBD.pdf.
- Turk, F. J., Z. S. Haddad, P.-E., Kirstetter, Y. You, and S. Ringerud (2018), An observationally based method for stratifying a priori passive microwave observations in a Bayesian-based precipitation retrieval framework, *Royal Meteor. Soc.*, doi:10.1002/qj.3203.
- 650 Xie, X., Y. Dong, W. Yu, W. Liu, H. Xu (2018), The effects of cloud liquid water on polarized radiative transfer calculations during snowfall at microwave band, 2018 IGARSS conference proceeding, doi:10.1109/IGARSS.2018.8517775.
- Yin, M., G. Liu, R. Honeyager, F. J. Turk (2017), Observed differences of triple-frequency radar signatures between snowflakes in stratiform and convective clouds, *J. Quant. Spec. and Rad. Trans.*, doi: 10.1016/j.jqsrt.2017.02.017.
- 655 Zeng, X., J. Gong, X. Li and D. L. Wu (2018), Analysis of tropical clouds with GMI and CloudSat data, PMM Science Team Meeting, Pheonix, AZ, 2018.
- Zeng, X., G. Skofronick-Jackson, L. Tian, A. E. Emory, W. S. Olson and R. A. Kroodsma (2019), Analysis of the global microwave polarization data of clouds. *Journal of Climate*, 32, 3–13, doi: 10.1175/JCLI-D-18-0293.1.

660

665

670

Region	Latitude bands	Season	Total #		High-PD	Mid-PD	Low-PD	Deep Convective
			Total Samples	#				
Tropics	30°S – 30°N	All-year	Ocn*3	779	16	100	644	19
			Lnd	320	0	86	227	7
NH	30°N – 50°N	NDJFM*1	Ocn	336	20	303	13	0
			Lnd	970	0	465	505	0
NH	30°N – 50°N	MJJAS*2	Ocn	107	15	85	7	0
			Lnd	153	1	121	28	3
SH	30°S – 50°S	NDJFM	Ocn	110	2	106	2	0
			Lnd	10	0	10	0	0
SH	30°S – 50°S	MJJAS	Ocn	181	7	170	3	1
			Lnd	74	1	70	3	0
Total				3040	62	1516	1432	30

675 *1: November – March

*2: May - September

*3: “Ocean” includes ocean and coastal footprints, determined by GMI surface flag.

Table 1: Collocation Statistics: total number of samples for each latitude band, season, surface condition (top: ocean and coastal; bottom: land), and scenario regime during March 2014 – October 2017. Note that total samples do not include collocations that are clear-sky or out of the boundaries of our definition of the four regimes.

680

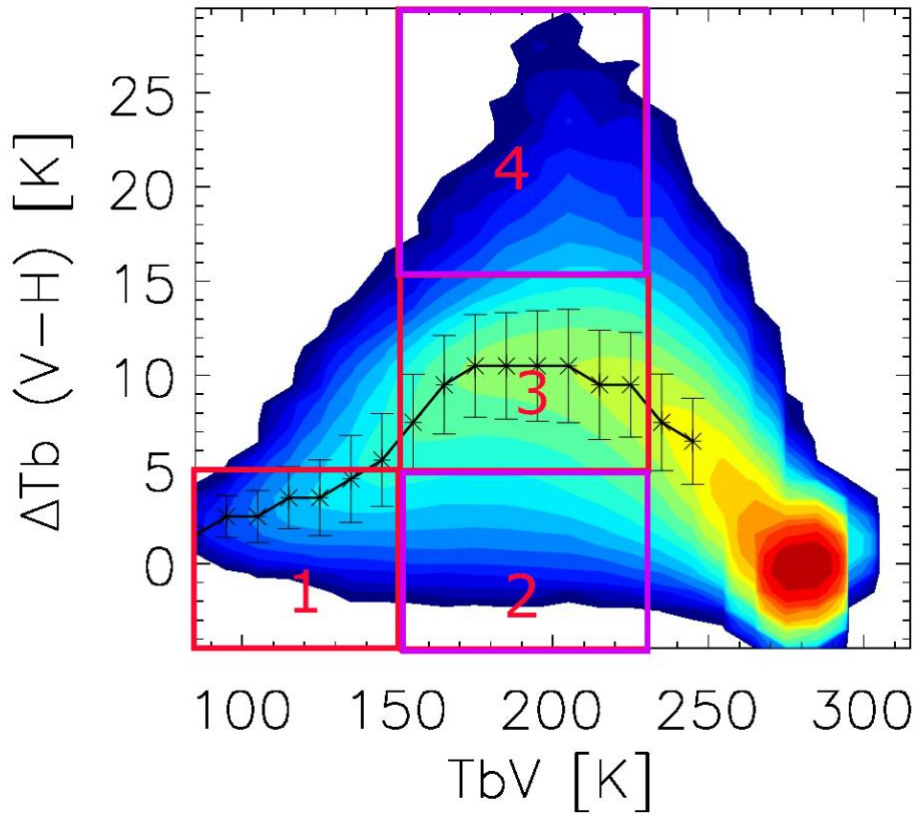
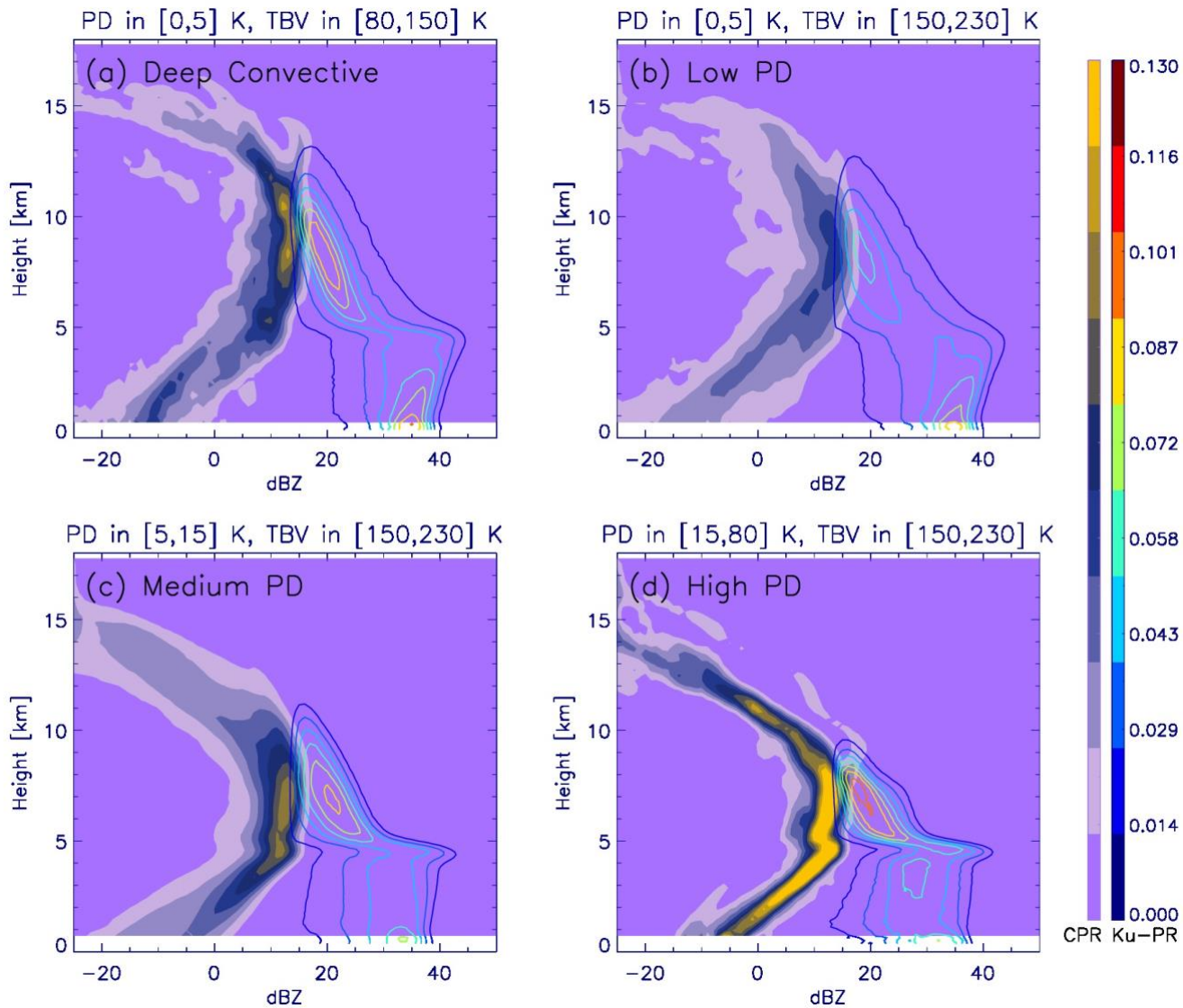
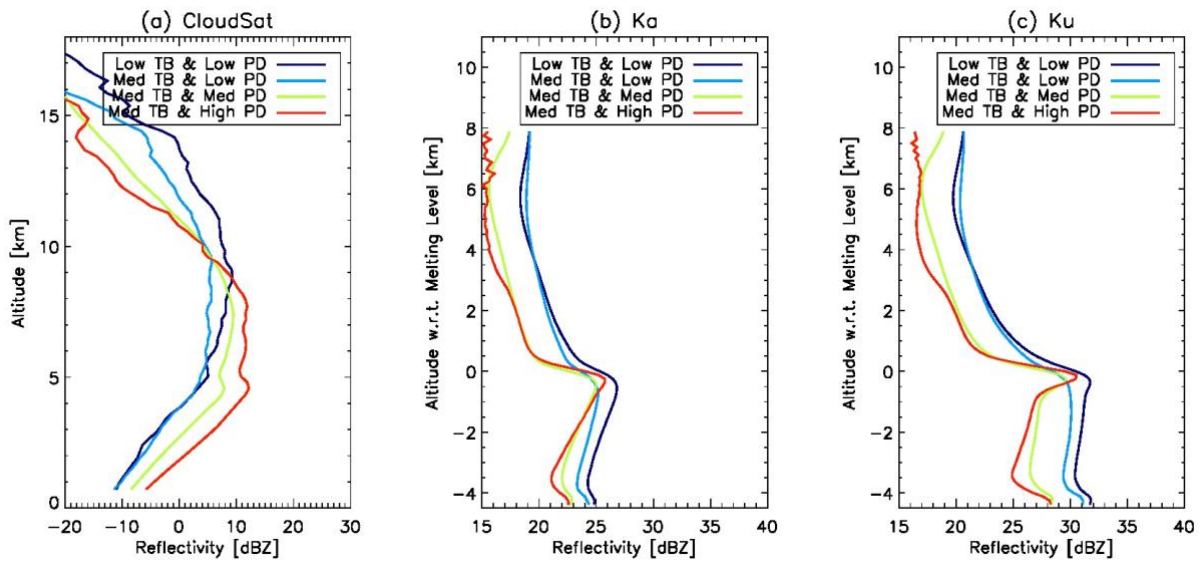


Figure 1: The definition of PD regimes according to the TBv and PD values: (1) deep convective; (2) low-PD; (3) medium-PD; and (4) high-PD. See text for values regarding the regime definition. Regime (2) low-PD and (4) high-PD, enclosed by purple rectangles, are the focus of study in this current work. Two-dimensional PDF contours are adapted from Fig. 3 of Gong and Wu [2017].

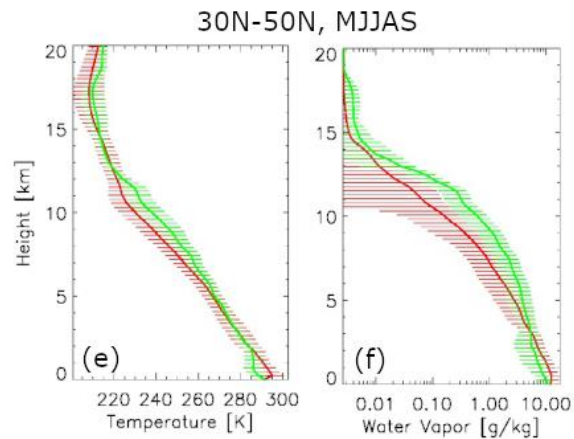
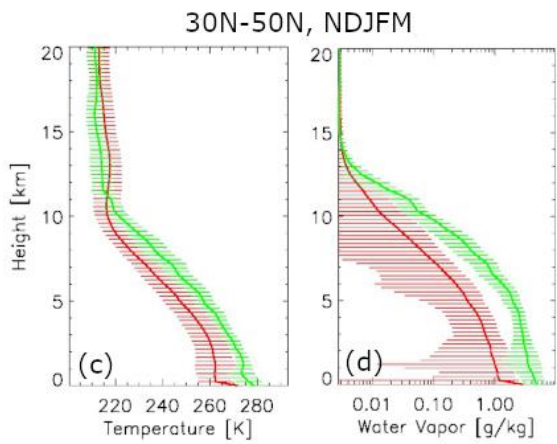
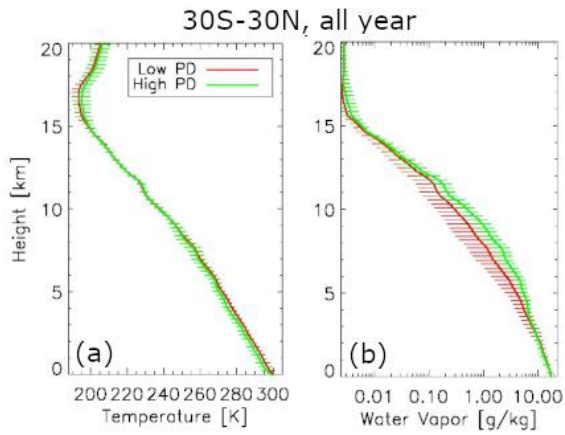


685

Figure 2: 2D PDFs from CloudSat (color shaded) and DPR-Ku (color contours) for the four regimes in Fig. 1 integrated from all tropical (30°S – 30°N) collocated scenes. (a)-(d) corresponds to regime#1 - #4 respectively. The contour scale is linear and relative to its maximum value.



690 **Figure 3: The collapsed 1-D view of Fig. 2 after weighted averaging along the axis of absolute reflectivity (i.e., x-axis) for (a) CloudSat, (b) DPR-Ka and (c) DPR-Ku. Note that the vertical axis for (a) is absolute altitude, whereas (b) and (c) are altitude with respect to melting level. The red (light blue) line is for the high-PD (low-PD) regime, respectively.**



695 **Figure 4: Temperature (left) and water vapor (right) profiles for “high-PD” (green) and “low-PD” (red) scenarios, respectively, for tropics [30°S – 30°N] averaged over years (top), Northern Hemisphere extended winter (middle panels, 30°N – 50°N, November-March), and Northern Hemisphere extended summer (bottom panels, May-September). Errorbars are also included in the same color for every other level.**

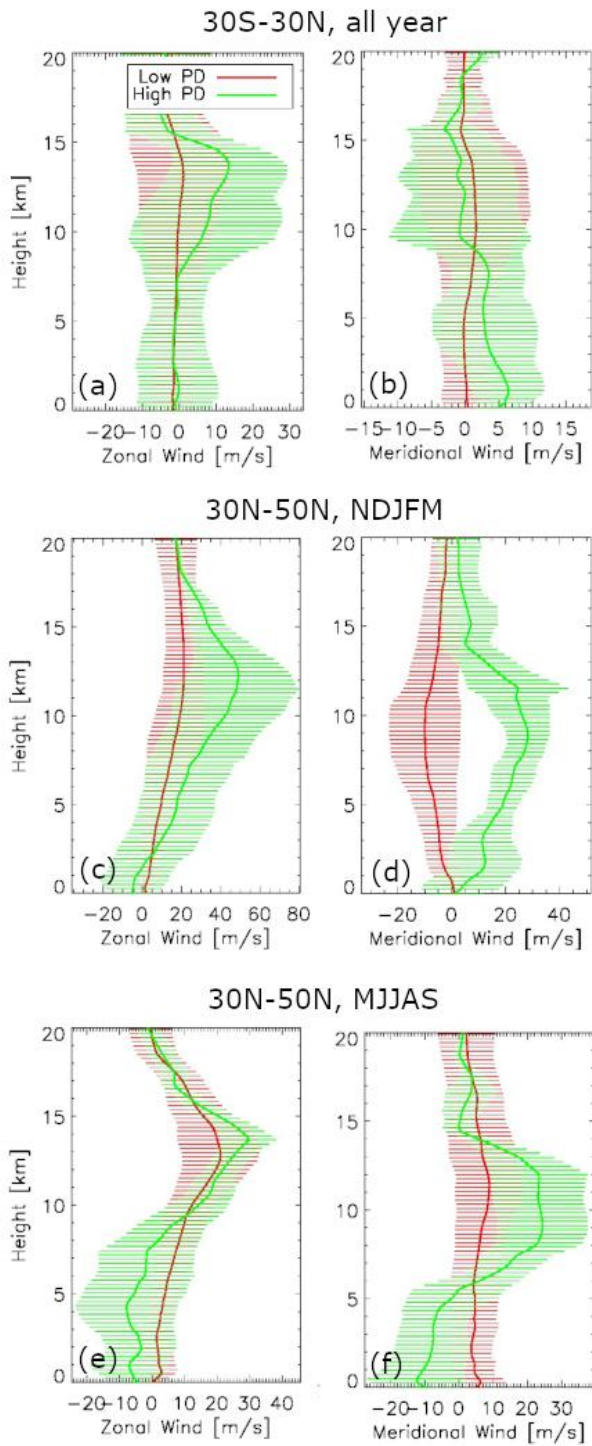
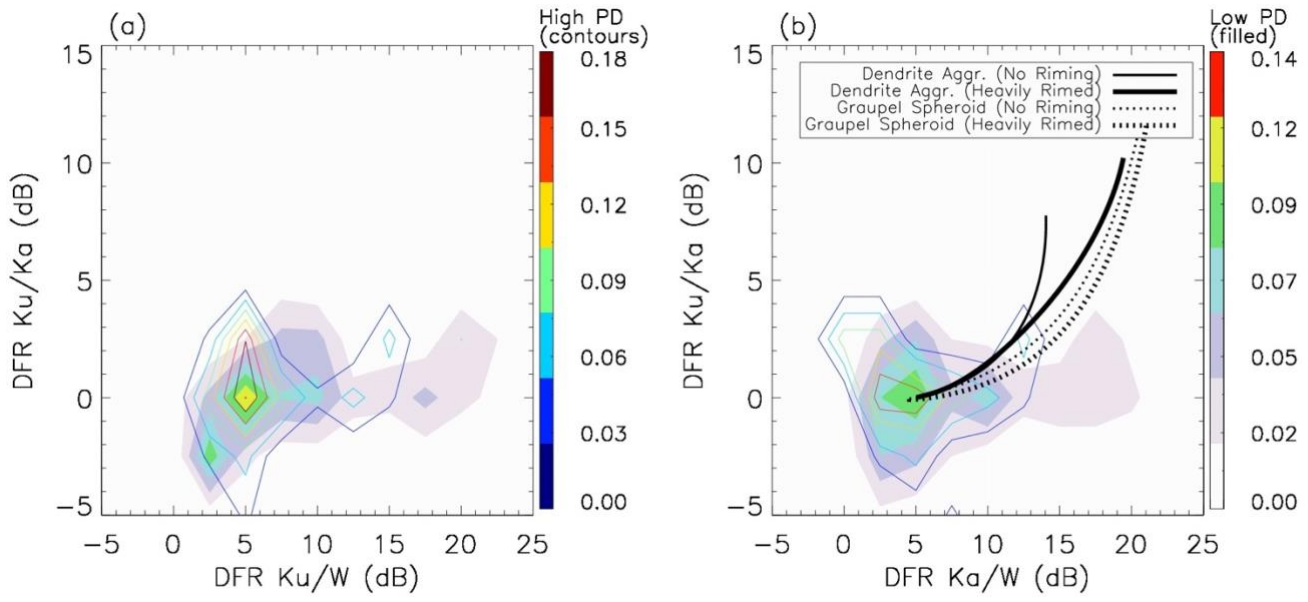


Figure 5: Same with Fig. 4, except for zonal wind (left) and meridional wind (right).



700

Figure 6: 2-D distribution of triple frequency DFR diagram from high-PD (rainbow-color contours) and low-PD (hue-color filled) regimes composited from all collocated CloudSat and DPR observations: (a) $DFR_{Ku/W}$ versus $DFR_{Ku/Ka}$; (b) $DFR_{Ka/W}$ versus $DFR_{Ku/Ka}$. The reflectivity observations are taken from the altitude range of 5.5 km – 15 km to minimize impacts from melting layer or rain. Model simulated dendrite (solid) and graupel spheroid (dotted) behaviors are overlaid on (b) for unrimed (thin) and heavily rimed (thick) cases. See Leinonen and Szyrmer [2015] for model and ice morphology details.

705

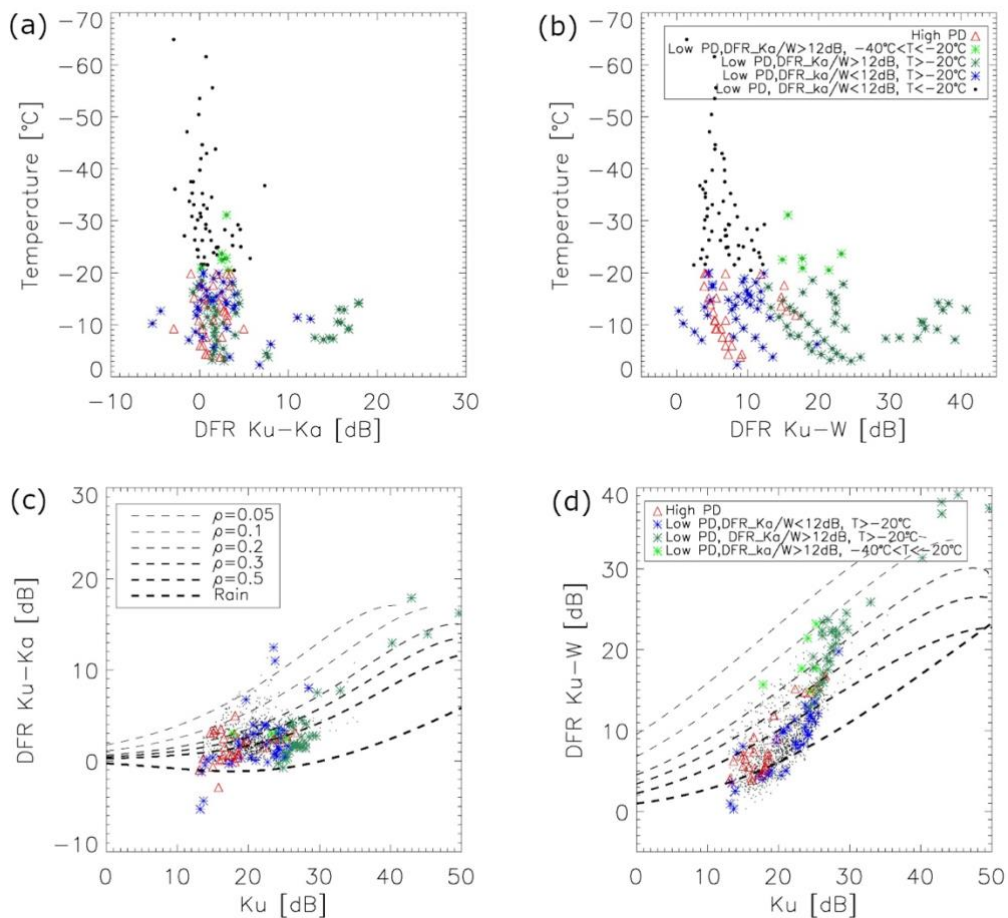
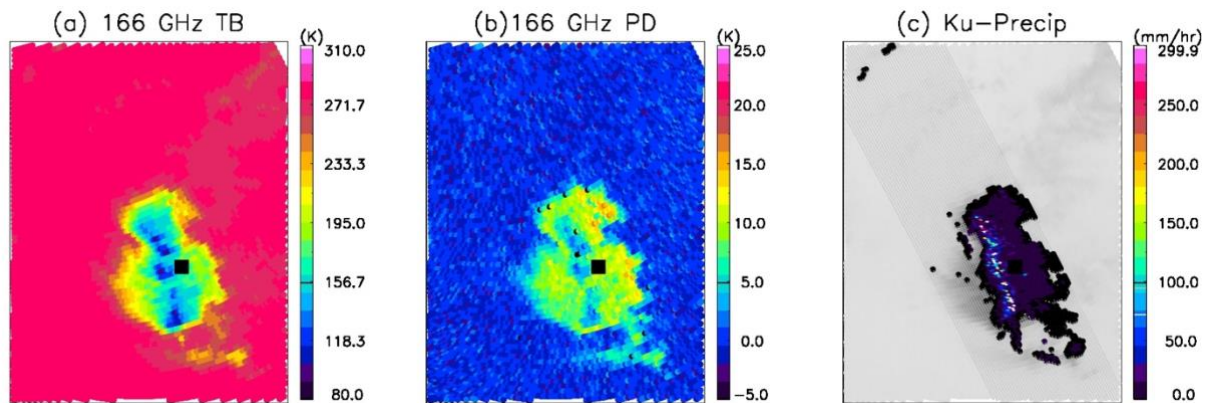
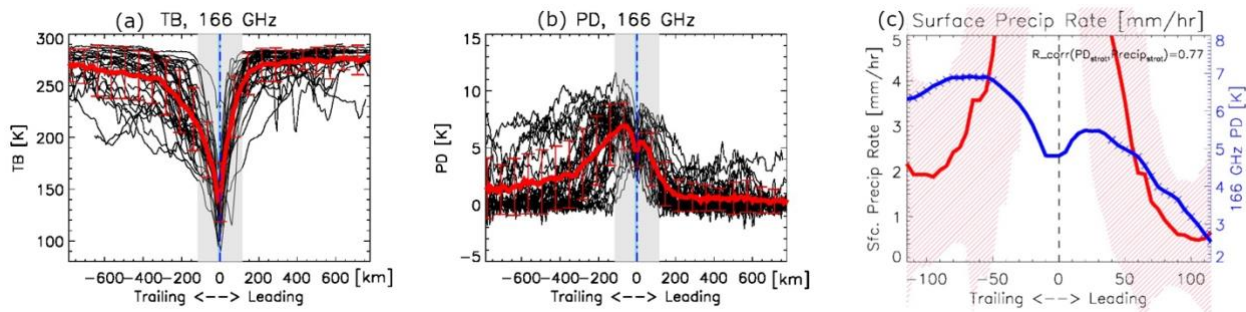


Figure 7: Scatter plots of DFR relationship to temperature (top) and to reflectivity (bottom) for high-PD observations (red triangle), low-PD with cold temperature and small $DFR_{Ka/W}$ (black dots), low-PD with warm temperature and small $DFR_{Ka/W}$ (blue star), low-PD with cold temperature and large $DFR_{Ka/W}$ (green star) and low-PD with warm temperature and large $DFR_{Ka/W}$ (green-blue star). Theoretical calculation of density isolines are overlaid in the bottom panels to facilitate our understanding the density (and habit) of each group of ice particles.

710

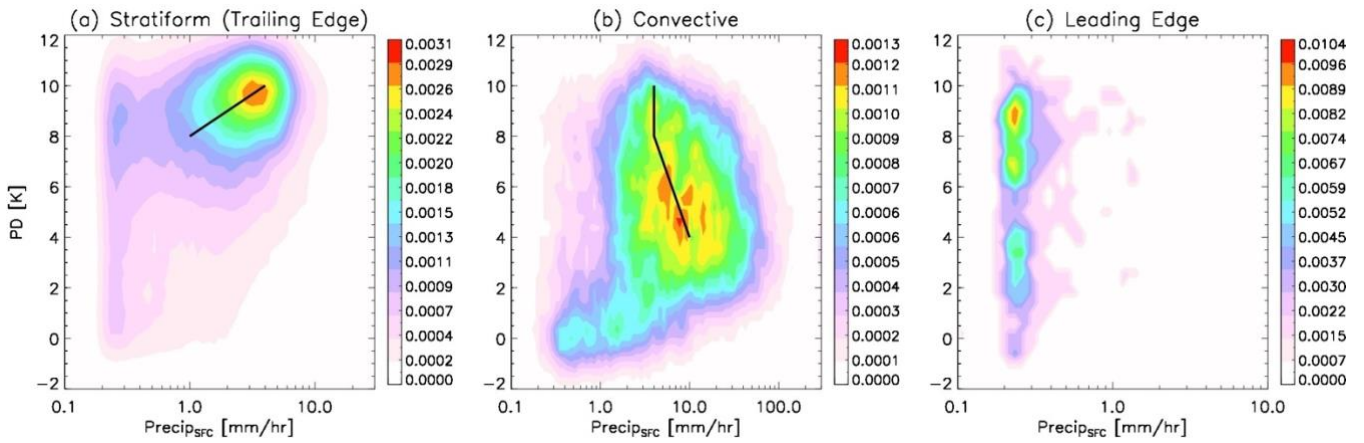


715 **Figure 8:** A squall line case captured by GMI and DPR exhibits larger PD behind (to the right) the deep convective front than in the leading edge (to the left). (a) 166 GHz TB; (b) 166 GHz PD, and (c) KuPR retrieved surface precipitation rate (color) on DPR swath (grey) overlaid on top of GMI 166 GHz PD (light grey). The black rectangle is just a reference point for easy inter-panel comparison. This squall line case occurred on July 20, 2015 (orbit #007908) over Chad, Africa.



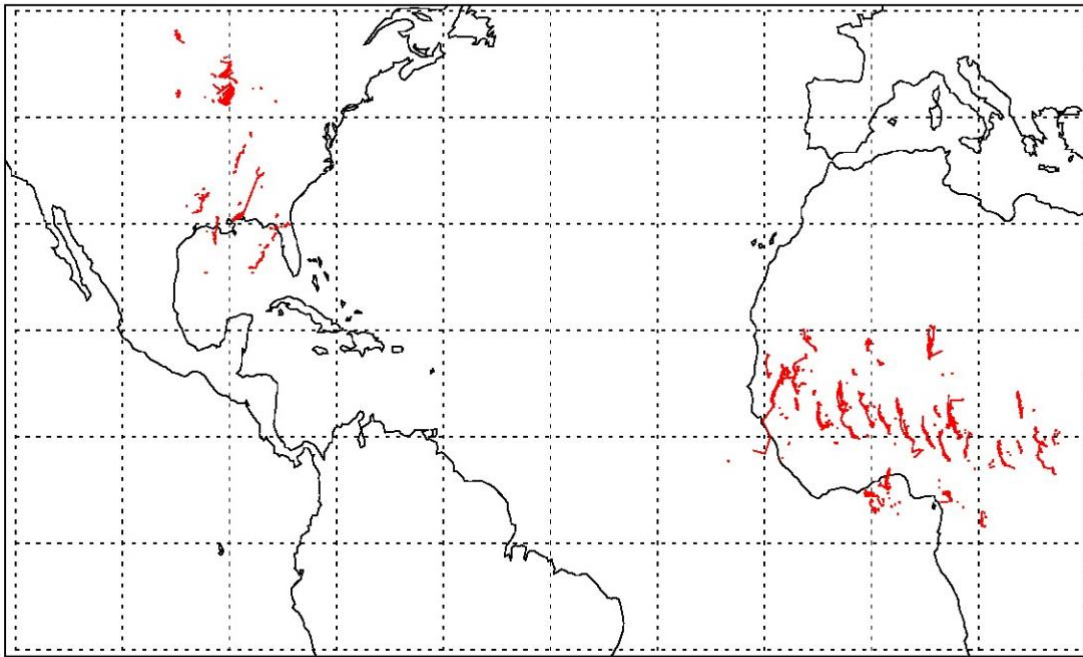
720 **Figure 9:** 166 GHz TB (a) and PD (b) distribution across the squall line center (0 at horizontal axis) for all 46 squall line cases (black) and their mean (thick red) and standard deviation (thin red error bars). The trailing edge is to the left and the leading edge is to the right. The squall line case details can be found in Table A1 in the Appendix. Light grey rectangles in (a) and (b) correspond to KuPR coverage. In (c), KuPR retrieved mean surface precipitation rate (PR_{sfc}) is shown as the thick red line across the squall line center with standard deviation shown in pink hatched areas. 166 GHz PD in the grey area in (b) is overlaid as the thick blue line in (c). Deep convective rainy footprints ($PR_{sfc} > 5\text{ mm/h}$) are excluded for plotting because our PD hypothesis only works in stratiform region. The Pearson rank correlation between PR_{sfc} and PD is 0.77 (significance at 99.9% confidence level) after excluding the deep convective footprints.

725



730 **Figure 10: Joint surface precipitation and 166 GHz PD distribution function (2D-PDF) in the (a) stratiform, (b) convective and (c) leading edge of the squall lines. DPR stratiform/convective/other flags are employed to differentiate different precipitation types.**

Appendix A: Complete list and geographic distribution of the selected squall line cases



735 **Figure A1: The geographic distribution of the 46 squall line cases that are selected. Red dots are the location of identified deep convective center (i.e., maximum PR_{sfc} while $PR_{sfc} > 25\text{mm/h}$ threshold) on each KuPR scan. Each scan swath is then aligned against this center location (setting as 0) to make the composites shown in Fig. 8 and Fig. A2.**

Orbit Number	Year	Month	Day	Longitude Center [°E]	Latitude Center [°N]
013718	2016	7	28	23.5	10.4
002737	2014	8	22	2.2	12.6
001476	2014	6	2	15.6	8.9
007202	2015	6	5	-0.2	5.7
001461	2014	6	1	5.1	4.3
019220	2017	7	17	18.8	8.5
018584	2017	6	6	-2.1	14.2
018891	2017	6	25	4.8	7
002169	2014	7	17	-12.9	14.6
007779	2015	7	12	4.3	12.5
002245	2014	7	21	7.2	15.3
002098	2014	7	12	8.3	10.2
018691	2017	6	13	11.4	12.1
019451	2017	7	31	5.9	10.4
012965	2016	6	9	24.3	8.1
002483	2014	8	6	-11.7	15.6
019021	2017	7	4	-0.8	13.3
002744	2014	8	23	-3.7	13.8
007908	2015	7	20	21.1	13
007640	2015	7	3	15.9	2.8
008225	2015	8	10	-4.2	9.9
002753	2014	8	23	-10.6	15.6
002107	2014	7	13	-1.2	15

002029	2014	7	8	23.5	9.3
018737	2017	6	16	11.1	5
013934	2016	8	11	0	18.7
002114	2014	7	13	-7	11.9
013097	2016	6	18	7.6	3.2
019267	2017	7	20	-4	13.3
002675	2014	8	18	13.2	8.5
001768	2014	6	21	14.4	3.7
002660	2014	8	17	8.4	18.9
001791	2014	6	22	0.8	3.8
007847	2015	7	16	9.7	12.8
013734	2016	7	29	9.9	9
014211	2016	8	29	-8.9	19.4
008308	2015	8	15	8.6	18.5
002851	2014	8	29	11.4	11.5
012959	2016	6	9	2.1	6
014225	2016	8	29	26	10.2
018861	2017	6	23	-10.1	13.3
013419	2016	7	9	26.6	7.3
008309	2015	8	15	-13.9	16.2
013795	2016	8	2	20.6	9.8
019245	2017	7	18	-7.2	11.5
008414	2015	8	22	-96.8	36.8

Table A1: Details about the 46 squall line cases we selected. First column lists the GPM orbit number. The 2nd-4th columns include year, month and day of the event, and the last two columns are the longitude and latitude of the reference center (i.e., black rectangle in Fig. 8 for easy comparison, not necessarily the storm center).

740

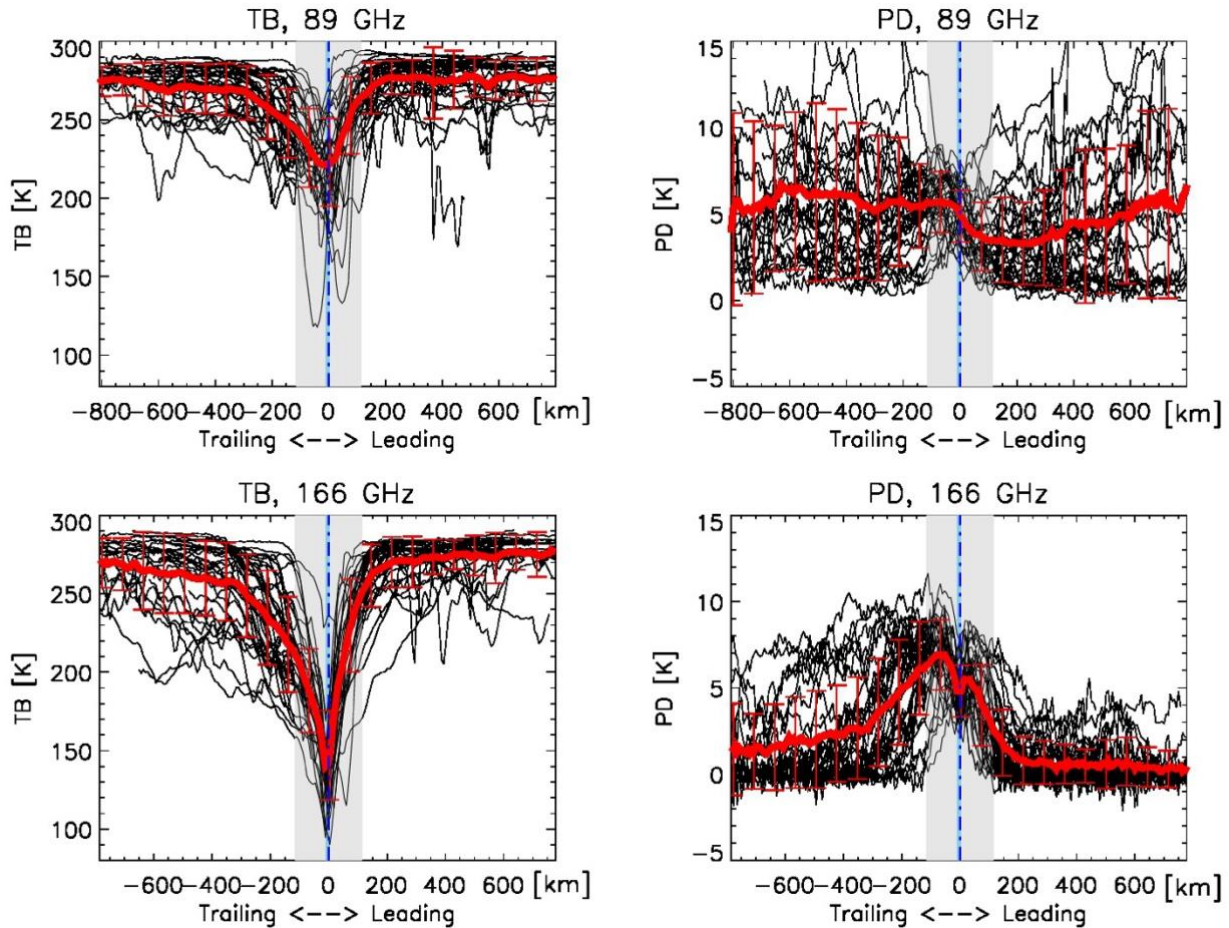


Figure A2: The bottom panels are the same with Fig. 9a and 9b, and the top panels are similar except for 89 GHz. One can see that the 89 GHz PD signal is not as clean as that at 166 GHz since the 89 GHz's PD is also strongly impacted by surface emissivity and liquid cloud/raindrop scattering.